TAMPEREEN TEKNILLINEN YLIOPISTO
TAMPERE UNIVERSITY OF TECHNOLOGY

SOUDABEH MORADI

FRONT-END DATA PROCESSING OF NEW POSITRON EMISSION TOMOGRAPHY DEMONSTRATOR

Master of Science Thesis

Examiners: Prof. Ulla Ruotsalainen
MSc Defne Us

Examiners and topic approved by
the Faculty council of Computing and
Electrical Engineering on 9 October 2013

ABSTRACT

TAMPERE UNIVERSITY OF TECHNOLOGY
Master's Degree Programme in Information Technology
Moradi, Soudabeh: **Front-end Data Processing of New Positron Emission Tomography Demonstrator**
Master of Science Thesis, 61 pages, 10 Appendix pages
January 2014
Major: Signal Processing
Examiners: Professor Ulla Ruotsalainen and MSc Defne Us
Keywords: PET, AX-PET, LYSO crystal, WLS strip, coincidence event, 3D co-ordinate, intramodular, intermodular, hit point, interaction point

Axial PET (AX-PET) is a novel geometrical concept for positron emission tomography (PET) based on stacks of long scintillating crystals aligned axially with the bore axis and layers of wavelength shifter (WLS) strips placed orthogonal to them. The novel structure allows for detection of depth of interaction using the stack of crystals with WLS strips thus avoiding the parallax error presented due to different depths of interaction in the crystals. Therefore, existing compromise between the sensitivity and spatial resolution in the conventional PET scanners is overcome and highly sensitive scanners with improved spatial resolution can be produced.

This thesis presents a new AX-PET demonstrator, which was built in Tampere University of Technology. The aim of the thesis is to define 3-dimensional coordinate system for this demonstrator as well as to determine the location of coincidence events in this system. The demonstrator consists of four modules each of which are containing two LYSO crystal layers and two layers of WLS strips aligned orthogonal to the crystals. The crystals and WLS strips are read individually. The signals coming from the crystals determine the X- and Y-coordinates of the hit and the signals from the WLS strips define its Z-coordinate. We created a small test data with MATLAB for examination of our methods. Subsequently, the coincidence events were determined using a coincidence window of 3 ns. For defining the location of the coincidence events, we first calculated its location inside the module (intramodular hit location) using the hit crystal and the corresponding WLS strip(s). Then we converted the location data to the scanner coordinate system (intermodular hit location). In order to speed up the positioning of the coincidence events, we created lookup tables such that 3D position of all possible interaction points were calculated beforehand and recorded in these tables. This way, it was not necessary to repeat all the calculations for positioning of each detected event, but the position was just selected from the lookup tables. This approach worked efficiently for positioning the coincidence events of our test data. The efficiency can be approved using a real test data, where large amount of coincidence events are detected.

PREFACE

This thesis was carried out in the Methods and Models for Biological Signals and Images (M^2oBSI) research group, at the Department of Signal Processing, Tampere University of Technology.

First, I would like to thank my thesis supervisors, Professor Ulla Ruotsalainen and MSc Defne Us for their wonderful advice and guidance throughout this work. I would also like to thank MSc Uygar Tuna for his excellent guidance and support during the first months of the work. I gratefully thank the Department of Signal Processing and Professor Ulla Ruotsalainen for organizing the funding for my work.

I would also like to express my special thanks to my parents Mohammad Ali Moradi and Fatemah Entezari for their endless supports throughout my life. My sincere thanks also go to my husband Mohammad Hashemi for his love and warm supports whenever I have needed. My very special thanks go to my daughter, Sahar for being the joy of my life and the delight in my days.

Finally, I thank my brothers, Samad Ali and Ramin for their support in all my life stage. My thanks also go to my sisters Elaheh and Elham, for being my best friends during my university studies.

Tampere, January 2014
Soudabeh Moradi

CONTENTS

LIST OF SYMBOLS AND ABBREVIATIONS

β^+	Positron
n	Neutron
p	Proton
v	Neutrino
m_e	Mass of electron
c	Speed of light
S	Sensitivity
A	Area
ε	Detector efficiency
μ	Linear attenuation coefficient
t	Thickness of detector
r	Radius of the detector ring
cps	Counts per second
μCi	Microcurie
kBq	kilobecquerel
Δt	Time difference
φ	Angle
τ	Coincidence timing window
P	Probability
σ	Resolution
E	Energy signal
Q	Charge signal
a_1, b_1, c_1	Constant
2D	Two Dimensional
3D	Three Dimensional
ADC	Analogue to Digital Conversion
APD	Avalanche Photodiode
AX-PET	Axial Positron Emission Tomography
CERN	European Organization for Nuclear Research

CoG	Center of Gravity
CT	Computerized Tomography
dSiPM	Digital Silicon Photomultiplier
DOI	Depth of Interaction
FDA	Food & Drugs Administration
FDG	Fluoro-deoxyglucose
FOV	Field of View
G-APD	Geiger mode Avalanche Photodiode
HRRT	High Resolution Research Tomograph, ECAT HRRT scanner (Siemens, Knoxville, U.S.A.)
HPD	Hybrid Photon Detectors
ICS	Inter Crystal Scatter
ID	Identification (label)
keV	Kilo electron Volt
LOR	Line of Response
LYSO	Lutetiumyttrium Oxyorthosilicate
MLEM	Maximum Likelihood Expectation Maximization
MPPC	Multi Pixel Photon Counters
MRI	Magnetic Resonance Imaging
pC	Pico coulomb
PC	Personal Computer
PET	Positron Emission Tomography
PMT	Photomultiplier Tube
SNR	Signal to Noise Ratio
SPECT	Single Photon Emission Computed Tomography
TOF	Time of Flight
WLS	Wavelength Shifter

1 INTRODUCTION

Over the last century medical imaging techniques have become an important part of the diagnostic and healthcare process. These techniques allow visualizing the structures and activities inside the human body in order to diagnose abnormalities in the patient's body and therefore to find the best course of treatment. Moreover, medical imaging is used also for management of a disease, which is already diagnosed or treated.

Medical imaging started with Radiology after the discovery of X-rays by Wilhelm Röntgen in 1895 [1]. Nowadays, variety of imaging techniques is added to the traditional radiology to assist in diagnostic of various diseases in humans. Some of these methods such as X-ray computerized tomography (X-ray CT) and magnetic resonance imaging (MRI) provide structural (anatomical) images of the organ of interest. On the other hand, functional images of the organs are produced by nuclear medicine imaging methods such as single photon emission tomography (SPECT) and positron emission tomography (PET).

In nuclear medicine approaches, radionuclides are combined with pharmaceutical compounds forming the radiopharmaceuticals. As a consequence of the injection of the prepared radiopharmaceutical to the patient, more pharmaceutical is delivered in certain organs or in cellular clusters, which are more active than the others [1]. Therefore, PET images are acquired by quantitative measurement of distribution of radiopharmaceutical and the temporal variation of this distribution.

PET is a nuclear medicine imaging, which makes use of positron-emitting isotopes for detection of certain functional processes in the body. It was primarily proposed in 1950 by researchers at the Massachusetts General Hospital in Boston and the Duke University in Durham [2]. However, the first PET system was used as a research tool in 1970 [3]. Clinical PET started with the advancement in technology and a wider application in the mid-1990s. In 1997 when approval of Fluoro-deoxyglucose (FDG), a radiopharmaceutical capable to trace the glucose metabolism, was granted by the US Food & Drugs Administration (FDA), PET-FDG became an established imaging tool for the assessment of many neoplasms as well as non-malignant diseases such as dementia, myocardial ischaemia, inflammation and infection.

Since PET provides excellent accuracy with respect to the other imaging techniques in assessment of certain oncological diseases including lung, colorectal, lymphomas, breast and head-and-neck cancers, it is considered to be one of the most important medical imaging tools [4]. Another desirable aspect of the PET system is the ability to be coupled with a CT system (PET/CT) or a MRI system (PET/MRI) resulting in both ana-

tomic and functional information of the body. Thus, a detailed view of moving organs or structures with more anatomical variation can be provided.

Nevertheless, performance of the currently used PET scanners needs to be improved in order to obtain images with good quality. One important factor affecting the image quality is spatial resolution of the scanner. A good spatial resolution for the system ensures precise localization of tiny structures especially in brain as well as detection of tumors at early stage. Another factor which increases the quality of image is detection efficiency of the detectors. Therefore, by using detectors with higher efficiency, the dose of radioactive injected to the patient can be reduced, keeping the image quality at the same level [5].

In conventional PET scanners scintillator detectors are arranged radially around the patient. This arrangement puts a tradeoff between the spatial resolution and detection efficiency of the scanner, as scanner efficiency can be increased using longer crystals, while longer crystals in absence of depth of interaction (DOI) of detected events, cause parallax error resulting in worse spatial resolution. Therefore, a new design for the scanner is developed. In the novel design, long crystals are arranged in axial direction (the patient direction) and a layer of wavelength shifter (WLS) strips is mounted above each crystal layer. Thus, the DOI information is determined by the signals obtained by the WLS strips. This way, the sensitivity and spatial resolution of the scanner can be improved independently [6].

Based on the novel axial concept, a new small demonstrator called as AvanTomography was constructed in Tampere University of Technology. This demonstrator can be used for preclinical studies as well as imaging of small parts of the body in clinical applications. This thesis studies the arrangement of different components in the AvanTomography demonstrator as well as the way of data storage and detection of coincidence events using the recorded data. However, main aim of the thesis is to describe a scanner coordinate system and to define 3-dimensional location of the coincidence events.

The thesis is subdivided in seven chapters. Next chapter represents the theoretical background of PET system including the physical principles of positron production and annihilation, the detected events, the factors that affect the performance of PET device and the correction ways in order to obtain better quality for the image. In third chapter, the axial PET concept and the acquired success comparing to the conventional PET design, are explained. Fourth chapter describes the assembly of the crystals and WLS strips in the AvanTomography demonstrator as well as the data acquisition process in it. In chapter five, the used methods in order to detect the coincidence events and also to define the position of the detected events are expressed. The results for the implemented methods are shown in sixth chapter. Finally, the last chapter concludes this work and proposes future improvements for the AvanTomography demonstrator.

2 PET BASICS

Tomography refers to an imaging technique that allows for visualization of the internal structures of an object without the superposition of over- or under-lying structures. Various developed medical imaging techniques result in tomographic images from internal parts of the body. Some examples of these methods are X-ray CT and MRI, which produce structural images of a certain organ or tissue as well as SPECT and PET, which visualize the metabolic processes in the organ of interest. Each such technique uses different source for obtaining the required information from the body. For instance, in the X-ray CT the x-ray source rotates around the patient, while MRI scanners use strong magnetic fields and radio waves to produce anatomical images of the body. As discussed in previous chapter, the functional methods (SPECT and PET) utilize radiopharmaceutical tracers injected to the patient in order to reflect their spatial distribution within the region of interest. The radioactivity used in SPECT is a single photon emitting isotope, while in PET a positron-emitting isotope is used. However, PET is more desirable technique in many clinical imaging applications because of the availability of numerous positron-emitter compounds as well as improved sensitivity and spatial resolution in the PET system compared to SPECT [7].

In this chapter, the physical background of PET, acquisition of the data and different parts of the PET scanner are briefly described. Moreover, data storage approaches and different data correction ways to achieve better resolution for the PET images are considered.

2.1 Physical principles of PET

In a PET scan, primarily a suitable radiopharmaceutical labeled with a positron-emitting radionuclide is produced. Afterwards, the prepared radiopharmaceutical is injected to the patient and the scan is started either immediately or after a delay to allow the tracer to be metabolized by the organ of interest.

Proton-emitting radionuclides are proton rich isotopes, which are unstable due to the unsuitable composition of protons and neutrons. They achieve the stability by converting a proton to a neutron, along with emission of a positron (β^+) and a neutrino (ν) [3]. This process is called as *beta plus decay* and is represented by the equation (2.1):

$$p \rightarrow n + \beta^+ + \nu, \tag{2.1}$$

where *p* indicates a proton, *n* is a neutron, β^+ is a positron and *v* is a neutrino. A positron is the antiparticle of the electron, which means that it has the same rest mass (m_e = 511 keV) as the electron with positive charge.

After the decay, the excess energy is shared between positron and neutrino, in the form of kinetic energy [2]. As positron passes through the matter, it loses its kinetic energy by ionizing surrounding molecules. Positron slows down and after passing a path called as positron *range*, it has the same speed as the surrounding matter. The positron range depends on its emission energy and electron density of the surrounding tissue [2]. Consequently, the positron combines with an electron resulting in the annihilation of both positron and electron. In the annihilation process, the entire mass of the electron–positron pair is converted into two 511 keV photons which travel in about 180º apart as illustrated in Figure 2.1 [3]. PET imaging is based on coincidence detection of these two photons by the photodetectors placed in the scanner.

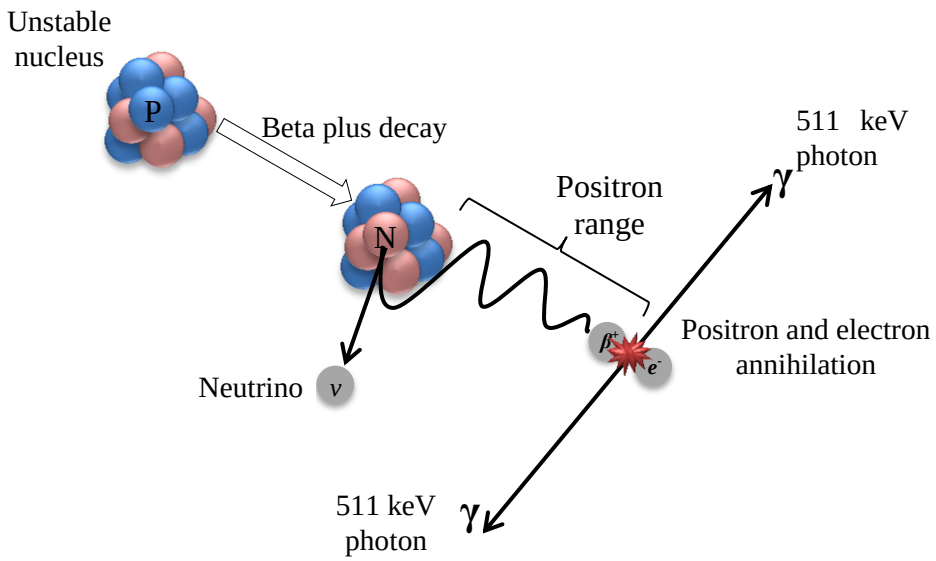

Figure 2.1. *Schematic representation of the positron emission and positron-electron annihilation processes. Inside the nucleus a proton decays to a neutron, a positron and a neutrino. The positron after traveling the positron range annihilates with a surrounding electron resulting in emission of two gamma photons, which travel in opposite direction.*

2.2 PET scanner

A typical PET scanner comprises of full or partial rings with a diameter of 80 to 100 cm. Each detector ring contains several blocks of detectors, where a block is composed of a rectangular bundle of scintillation crystals coupled to several photomultiplier tubes (PMT) as shown in Figure 2.2 (a) [8].

When annihilation occurs, the produced photons travel towards the scanner and hit the scintillator crystals located in the blocks. In the scintillator crystal material, the outer

electronic states are disposed in series bands of energy. The last filled band is called valence band (lower energy) and the first unfilled band is called conduction band (higher energy). The photon deposits its energy, while it hits the crystal. At this instant, some electrons in the valence band gain the released energy and get excited into the conduction band. Since this state is not as stable as the ground state, the electron returns to its ground state and releases its energy in the form of visible light. This process is called *scintillation*, hence the name of these detectors. The scintillation photons are emitted isotropically and their amount is proportional to the amount of released energy in the crystal. Subsequently, PMTs capture the emitted light photons and convert them to electrical pulses [2, 9].

The scintillation process in the detectors results in a large number of light photons, say, 10000. The ratio of the photons in the PMTs varies as scintillation moves from crystals on one side of the block to crystals on the other side [10]. This ratio is used for determining the location (X and Y-coordinates) of the hit and thus defining the interaction crystal using equations 2.2 and 2.3:

$$X = \frac{B + C - (A + D)}{A + B + C + D} \tag{2.2}$$

$$Y = \frac{C + D - (A + B)}{A + B + C + D} \tag{2.3}$$

where A, B, C and D are pulses from the four PMTs as shown in the Figure 2.2 (a). This way of determination of hit location is called Anger logic.

In order to detect the photons coming from the same annihilation, each detector element (crystal) is connected by a coincidence circuit to a set of opposite detector elements. The number of connected detectors in coincidence to a detector determines the acceptable angle (in the transaxial plane) of it, and using the acceptable angles of all detectors in the ring, the transaxial field of view (FOV) in the scanner is defined [3]. This is illustrated in Figure 2.2 (b).

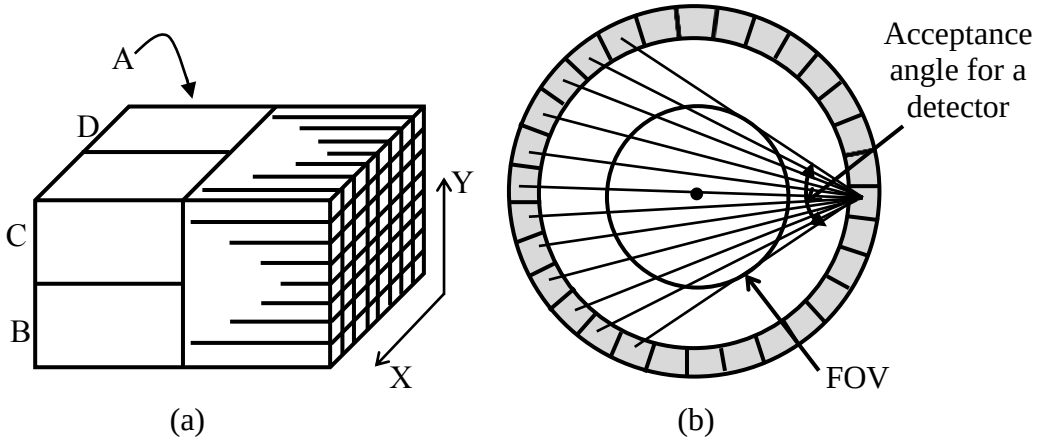

Figure 2.2. *PET scanner. (a) A block of photodetectors containing 8×8 crystals coupled to four PMTs. (b) Acceptable angle of a detector and determined FOV using the acceptance angle of all detectors.*

Scintillator crystals

Scintillator detectors used in PET scanner must have four main characteristics in order to acquire high quality images. These are: great stopping power for 511 keV photons, short scintillation decay time, high light output per keV photon energy and good energy resolution [3]. The stopping power of the scintillator is defined as mean distance travelled by the photon before it deposits all of its energy. It depends on the density and effective atomic number of the detector material. The decay time of the scintillator is the rate at which it emits light after the excitation. A detector with high light output produces a precise pulse, which results in a better energy resolution. The intrinsic energy resolution of a detector is affected by inhomogeneities in its structure and by the random variations in the produced light inside it. The energy resolution of different scintillator detectors at 511 keV varies from 6% to 20% for the normal integration time of pulse formation which is around few microseconds. However, in PET imaging a shorter integration time is used in order to exclude the random coincidences, thus smaller numbers of photoelectrons are collected to form the pulse which leads to a degradation in energy resolution (10% to 25%) [3].

A photon may interact with the scintillator detector via photoelectric effect, Compton scattering or not interact at all [2]. A photoelectric effect arises when the photon releases all its energy due to interaction. Instead, in Compton scattering it delivers only part of its energy and experiences a change in direction as shown in the Figure 2.3. The photon may also undergo multiple Compton scatters before it either escapes the detector or is absorbed through the photoelectric effect. Compton scattering does not occur only in the crystals as it may happen inside the object as well.

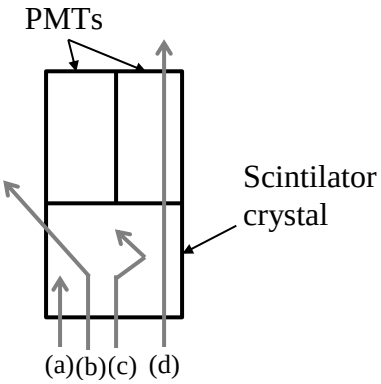

Figure 2.3. *Illustration of different type of photon interaction with the scintillator crystals. (a) Photoelectric effect. (b) Compton scattering. (c) Multiple Compton scattering. (d) Photon escapes the detector. Adapted from [2].*

Photodetectors

Photomultiplier tubes (PMT) are the most commonly used photodetectors in PET technology. However, there is a physical size constraint, which limits the production of very small PMTs [9, 11]. Thus, each photomultiplier is coupled to a block of crystals as shown in Figure 2.2 (a). However, one to one coupling of the crystal and photodetector is more reliable, with better temporal and energy resolution as well as shorter dead time [11]. Therefore, photodetectors of very small size called Avalanche photodiodes (APD) were developed. These are small enough to be coupled to a crystal instead of a block of crystals. In addition, they provide an internal amplification of the signal thereby improving the signal-to-noise (SNR) ratio [9]. However, APDs are very temperature dependent and have a limited availability due to their high cost [11].

2.3 Coincidence detection

Once annihilation occurs, generated gamma photons travel towards the scintillation detectors in the scanner. To detect the photons originating the same annihilation, a fixed time window called *coincidence time window* is used. The length of this window depends on timing resolution of the system. In other words, as timing resolution of the system represents the variability in detection time of the events, it is taken into account while selecting a coincidence time window [9]. The timing resolution in turn depends on decay time of the scintillator crystals. I.e. scintillator crystals with a short decay time result in generation of fast signals and thus a better timing resolution [9].

In a PET scanner, as annihilation occurs anywhere within the scanner FOV, the distance traveled by the two emitted photons before the detection may differ as much as the scanner diameter. Thus, for a scanner of diameter of one meter and using the value of speed of light c=30 cm/ns, a maximum time difference of 3-4 ns is calculated between the detection of the photons emitted from the same point. Therefore, the coincidence time window of a PET system needs to be increased even more than requirements of the timing resolution [9]. For instance, using an extremely fast scintillator such as

BaF_2 the timing resolution is very accurate, but the coincidence window cannot be smaller than 3-4 ns because of the difference in arrival times of the two photons emitted at the edge of the scanner FOV.

When two photons are detected within the same coincidence time window, a *coincidence event* will be recorded. Since annihilation photons are emitted about 180º apart, a recorded coincidence indicates a line connecting the two detectors called *line of response* (LOR). The set of all detected LORs constitutes the raw data that will be used afterwards for image reconstruction.

The selected coincidence window affects the detection of the photons from the same annihilation (a true LOR). In addition, there are other factors such as Compton scattering and photon attenuation that influence the localization of a true LOR. Depending on these factors, several coincidence event types may be detected. These events are explained below.

Coincidence event types

The desired events occurred in PET are *true coincidence events*, where both annihilation photons in the same coincidence window and without any scattering or any energy loss are detected (see Figure 2.4 (a)). However, due to limitations of detectors and possible interaction of the photon inside the subject or in the detectors, some unwanted events such as random coincidences, scatter coincidences and multiple coincidences may occur.

If two annihilations occur at approximately same time, they result in emission of four photons. Two of these photons from different annihilations may be detected in the same coincidence time window, while the other two photons may be lost due to the finite length of the window or because of attenuation in the subject (see Figure 2.4 (b)). Therefore, detected photons are considered to come from the same annihilation and are recorded as a coincidence. Such event is referred to as *random coincidence* or *accidental coincidence*. The number of random coincidences can be reduced using a smaller coincidence window. As determined LORs from random coincidences cannot be used for defining the annihilation position, they are eliminated and the dataset is reorganized using a proper correction method (see Section 2.7).

A *scatter coincidence* arises when one or both of the gamma rays from single positron annihilation undergo a Compton interaction. As direction of the photon changes during the Compton scattering, it is very likely that the resulting coincidence event is assigned to a wrong LOR as shown in Figure 2.4 (c) [12]. Therefore, in order to determine the actual LOR of the occurred event, a suitable correction method should be utilized.

Another type of undesired detected events is *multiple coincidences*. They occur in the same way as random events, but here three or four photons from two annihilations are detected inside the same coincidence window as illustrated in Figure 2.4 (d). Since it is not possible to discover the true coincidence pair between the three photons and decide the actual LOR, multiple events are discarded.

In addition to coincidence events, sometimes only one of the annihilation photons is registered while the other one is missing. The partner photon may be on a trajectory that does not intersect a detector, it may not deposit enough energy to be detected or, may not interact at all. Such events referred as *single events* are not accepted as true counts by PET system, but they are used for random and scatter corrections.

All registered events are referred to as *prompt events* i.e. they consist of true, scattered and random events, where only true events carry spatial information regarding the distribution of radiotracer in the body. Therefore, for each LOR the fraction of scatter and random events has to be estimated and subtracted from the measured prompts to yield the net true events for it [13].

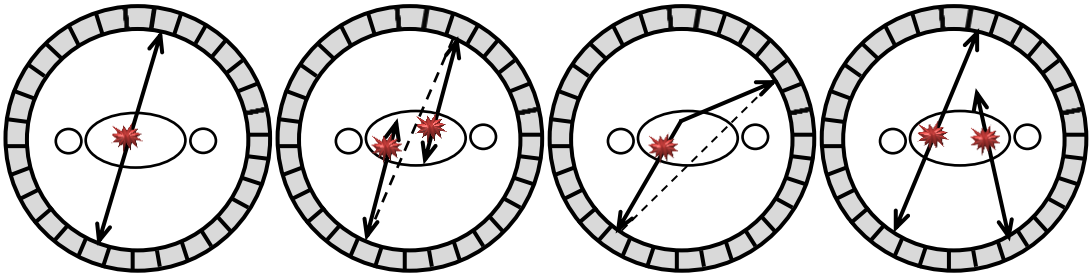

Figure 2.4. *Coincidence event types in PET. (a) True event. (b) Random event, the defined LOR is assigned with a dotted line. (c) Scatter event, the dotted line indicates the determined LOR. (d) Multiple events.*

2.4 Performance of the scanner

Since PET imaging has an important role in diagnosis and staging of malignant diseases, performance of the imaging technology is significant. In this section, a number of factors which affect the performance of a PET scanner are discussed.

Spatial resolution

Spatial resolution is defined as the ability of a scanner to reproduce the details of radionuclide distribution. The more details a scanner reproduces, the better spatial resolution it has. It is specified as full width at half maximum (FWHM) of point spread (PSF) function. The PSF describes the response of the imaging system to a point source. Figure 2.5 shows an example of a PSF curve and the resulted FWHM resolution. [14]

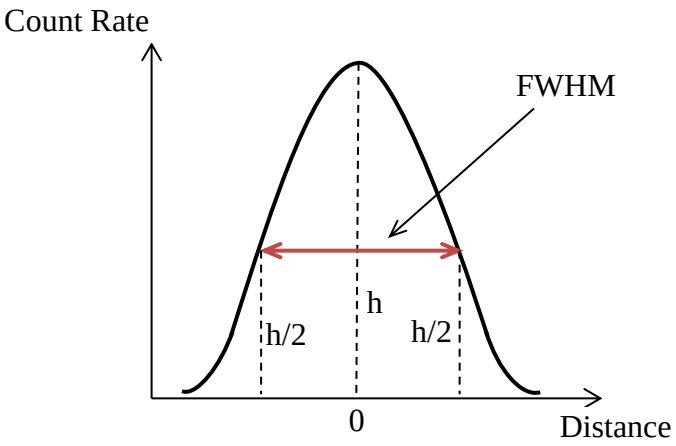

Figure 2.5. *Definition of the FWHM resolution. The FWHM is defined as the width of the PSF curve at half of its maximum.*

Many factors affect the spatial resolution of a PET system. One important factor is the depth at which the photon interacts with the scintillator crystal (i.e. releases its energy) called as depth of interaction (DOI). When a photon enters a crystal, it travels a short distance until it deposits all its energy. Thus, the actual location of the energy deposition is not the entrance surface of the detector, but it is projected to that surface [8]. Moreover, a photon that hits a detector with an oblique angle with respect to its axis may penetrate through first detector and be detected in an adjacent one as illustrated in Figure 2.6 [15]. This leads to a wrong localization of the LOR called *parallax error* or *radiation elongation*, which results in blurring in the reconstructed image. The parallax error is absent in the center of FOV as photons enter the detectors perpendicular to the face and it increases with distance of the event from the center of FOV as shown in Figure 2.6 [13, 8, 15]. A scintillator material with high stopping power is desirable for reducing the parallax error as it diminishes the distance traveled by the photon inside the crystal. So, one way to avoid this error is to use thin crystals with high stopping power, thus decreasing the distance traveled by the photon inside the crystal. Since using thin crystals decreases the scanner sensitivity; in order to separate this dependency between sensitivity and parallax error, an accurate measurement of the DOI in the crystal is required [8].

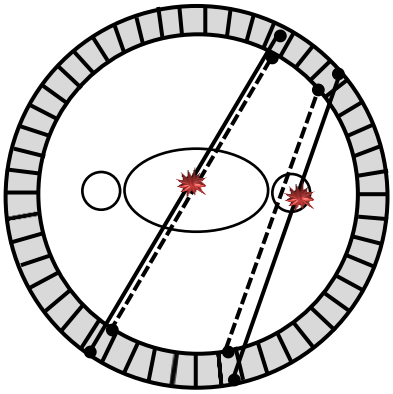

Figure 2.6. *Illustration of the parallax error influencing annihilation points far from the scanner center. The dotted line shows the defined LOR by the system and the continuous line shows the actual LOR produced by the annihilation.*

Positron *range* and *non-colinearity* of the annihilation photons are two other factors that induce errors in localization of LOR and so limit the accessible spatial resolution of a PET scanner [13]. When a radionuclide decay occurs, the emitted positron travels a short distance called as positron range after which it annihilates with a surrounding electron. Since a PET scanner detects the location of the annihilation and not the location of the positron emission, an error occures in positioning of the location of the positron emision which results to degradation of the spatial resolution [3]. Non-collinearity of the annihilation photons arises when they are not emitted (exactly) collinearly from the annihilation point because of some residual momentum of the positron at the end of positron range. The photons non-colinearity leads to determination of LOR, which does not intersect the point of annihilation and thus degrading the spatial resolution of the image. The resulted error deteriorates with increasing the distance between the detectors. Consequently, contribution of non-colinearity worsens the resolution in the scanner with larger diameter [3].

Energy resolution

Energy resolution of a PET detector represents its ability to distinguish between radiations at different energies [8]. A good energy resolution enables the reduction of the scatter coincidences in a PET system. Since scatter involves a loss in the energy of the photon, using an energy-gating technique around the photopeak in the energy spectrum allows to reject a number of scatter coincidences. Therefore, by using detectors with good energy resolution, a very narrow energy gate can be chosen and so scatter coincidences can be rejected more accurately [8].

Sensitivity

In PET, quality of the image is proportional to the number of detected coincidence events by detectors. The factors affecting the number of the detected events are the amount of injected radioactivity, the fraction of the activity that reaches the tissue of interest, the imaging time and the sensitivity of the scanner. Scanner sensitivity is de-

fined as the number of events detected and recorded by the scanner per unit of radioactive concentration in the tissue (counts per second per microcurie). Since the amount of the activity that can be administered to the patient and the imaging time are limited, the system sensitivity is a key factor to attain high quality images [13].

The sensitivity of the scanner depends on several factors including efficiency of the detectors at 511 keV, geometric efficiency of the scanner, dead time of the system (see Section 2.7, Dead time correction), and the coincidence time window and energy windows applied to the data [3, 13]. Detection efficiency of a detector depends on its scintillation decay time and stopping power (see Section 2.2, Scintillator crystals) dependent on the thickness of the detector material. The geometric efficiency of the scanner is defined by the overall solid angle coverage of the detectors by the source of activity. As distance between the source and detectors increases, the solid angle at detectors becomes smaller, thus decreasing the geometric efficiency of the scanner. Therefore, increasing the scanner diameter reduces the solid angle and in turn the geometric efficiency of the scanner, which results in reduction of the system sensitivity. In addition, the sensitivity increases with increment of the number of rings in the scanner. Sensitivity of a single ring PET scanner with certain detector material can be expressed using equation (2.4) [3]:

$$S = \frac{A \cdot \varepsilon^2 \cdot e^{-\mu t} \cdot 3.7 \times 10^4}{4\pi r^2} (cps/\mu Ci), \tag{2.4}$$

where A represents detector area seen by a point source, ε is detector efficiency, μ is linear attenuation coefficient of 511 keV photon in detector material, and t and r represent the thickness of the detector and radius of the detector ring respectively.

2.5 Time of flight PET

As discussed before, in conventional PET systems, the actual position of the annihilation is not detected, but the line along which the annihilation has been occurred is identified. In order to detect the annihilation point and thus discover the actual location of the radioactive source, the so called time of flight (TOF) method can be used [13]. The TOF method in PET yields to increase in SNR and also much lower random coincidences than that of non-TOF PET (as a coincidence window of smaller size can be used). This approach uses the difference of arrival times of the photons at the detectors to calculate the annihilation location using the equation (2.5):

$$d = \frac{\Delta t \times c}{2}, \tag{2.5}$$

where *d* is distance of the annihilation point to the midpoint of the LOR (see Figure 2.7), Δt represents the difference in arrival time of the photons and *c* indicates the speed of light (30 cm/ns).

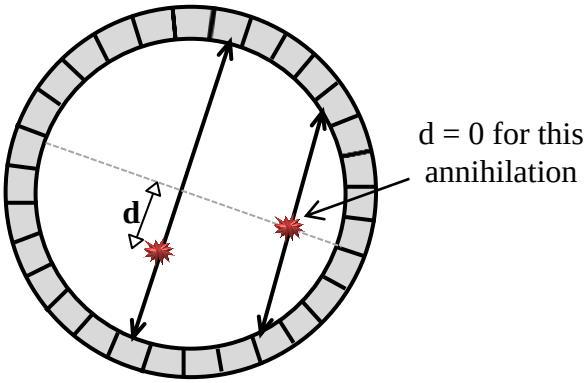

Figure 2.7. *Detection of the annihilation point using TOF method. The dotted line goes through the midpoint of the LORs. When annihilation occurs at the midpoint of the LOR, the parameter d in equation (2.5) gets zero value.*

In practice, this method is very difficult and costly to implement due to very small time difference to be measured. Thus, it is rarely used and actually the currently manufactured PET scanners do not use it.

2.6 Data acquisition

PET data acquisition can be accomplished in 2-dimensional (2D) and 3-dimensional (3D) modes depending on the design of the scanner.

In 2D acquisition, thin annular septa made of tungsten or lead is placed between the detector rings. This way, data acquisition is limited to coincidences detected within the same detector ring (direct plane) shown in Figure 2.8 (a). In order to improve the sensitivity, coincidences from the adjacent rings are also allowed (cross plane) as shown in figure. Using of septa in 2D mode results in fewer scattered and random counts. However, it also reduces the sensitivity as coincidences between all detector rings are forbidden [2].

In order to increase the system sensitivity, the septa is retracted or not included in 3D acquisition (see Figure 2.8 (b)). This way, all coincidences from all detector pairs are recorded, thus increasing the sensitivity by a factor of ~6 with respect to the 2D acquisition mode. However, absence of septa in 3D mode leads to more scatter and random events resulting in worse spatial resolution as well as requires more computer memory [2]. As a trade-off, the angle of acceptance can be limited, thus cutting off the random and scattered events at the cost of sensitivity. In other words, each detector can be connected to a fewer number of opposite detectors. In 3D acquisition mode the axial sensitivity is greatest at the center of FOV and continuously decreases towards the periphery [3]. Therefore, it is necessary to place the structures of interest as close to the center of the axial FOV as possible.

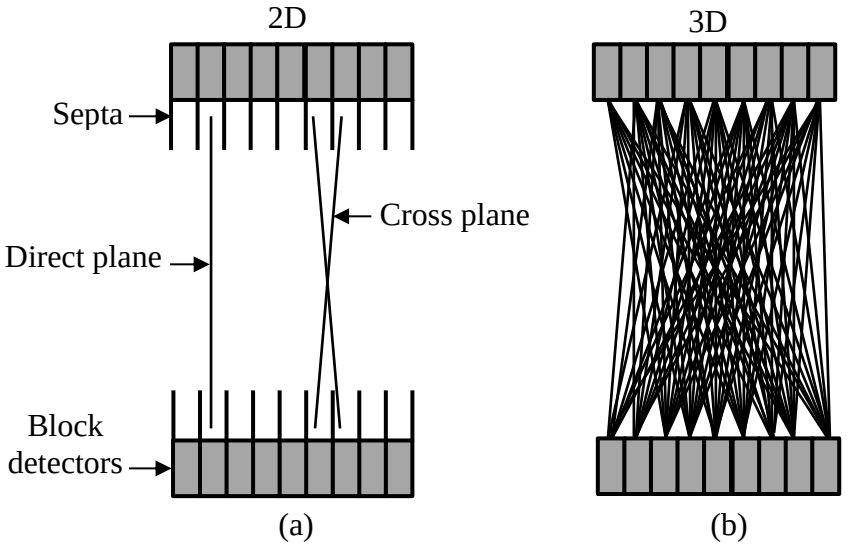

Figure 2.8. *PET data acquisition modes. (a) 2 dimensional. (b) 3 dimensional.*

2.6.1 Sinogram construction

In PET, the determined LORs from the coincidence events are stored in form of a sinogram. Each LOR is defined by the angle of orientation (φ) and its distance from the center of the gantry (s). A projection, p(s, φ), is formed from integration along all parallel LORs with the same angle. The projections from different angles ($0 \le \varphi \le 2\pi$) are organized into a sinogram such that each projection fills a single row in the sinogram. As a result, a single point in the object traces a sinusoid in the sinogram. This is illustrated in Figure 2.9.

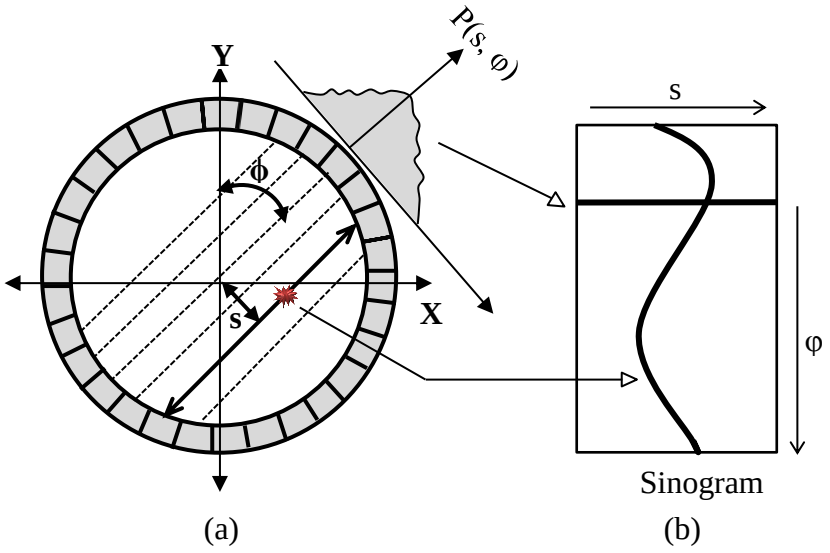

Figure 2.9. *Sinogram construction by integrating LORs at different projections. (a) Integration along all parallel LORs (the LORs with the same φ and different s) result in a projection P(s, φ), which fills a single line in the sinogram. (b)Sinogram for the annihilation point given in (a).*

2.6.2 Data representation ways

The PET data can be stored in two different ways: *histogram mode* (sinogram) or *list mode*. In histogram mode (or frame mode), position of the LOR for each detector pair is assigned in the sinogram before the acquisition. Consequently, during the acquisition, for each detected coincidence event, corresponding LOR is determined and value of the relevant pixel is incremented by 1 [3]. The histogram mode is efficient for storing of data in static scans, where the data is acquired over a fixed length of time and results in a single frame. However, in dynamic studies, the data are collected over a sequence of continuous acquisitions, where each one can take from 10 s to over 20 min. The data from each of the frames is then reconstructed to form a set of images [16]. Histogram mode is not efficient in dynamic imaging as scans with different durations result in different amount of detected events. In other words, reserving a sinogram pixel for each detector pair can result in large number of zero values in short scans. This is noticeable in modern 3D scanners, where the number of detector pairs is very high and many of detector pairs may not detect any event during the acquisition [13].

In order to use the memory efficiently as well as to extend the flexibility in data processing after the acquisition, list mode technique can be used. In list mode, the events detected in a certain time slots for example 1 s are written individually to a file. Each written event in such file contains information on the location of the interaction point of the two annihilation photons with the crystal, the time of the interaction, energy of the gamma photons, etc. The amount of information saved in an event word depends on the specified length of the word in a particular system [7]. The list mode data can be rebinned into sinograms after the acquisition and be used further for image reconstruction. List mode data representation has also other clinical benefits such as real time motion correction and improvement of image quality [17].

2.7 Data correction types

In a good quality PET image, each voxel value represents the true tissue activity concentration. As described before, random and scatter coincidences recorded in the acquired data result in incorrect localization of LOR, causing degradation in the spatial resolution of the image. Moreover, there are other resolution degrading factors such as photon attenuation in the matter, detector dead time and positron range. Therefore, after acquisition, the dataset has to be modified using proper correction methods. In this section, the most important corrections required for PET data are explained. The corrections are typically applied to the sinograms as a series of multiplicative factors before the image reconstruction.

Random correction

Random events occur when two photons arising from different annihilations are detected in the same coincidence window and are assumed to be from the same annihilation.

These events add a uniform background in the reconstructed image, thus suppressing contrast and distorting the relation between image intensity and actual activity distribution in the image [18]. The rate of random events along a specific LOR is calculated using equation (2.4):

$$R_{LOR} = \tau C_1 C_2, \tag{2.4}$$

where τ is the coincidence time window duration in nanoseconds and C_1 and C_2 are count rates of the single events on each of the two detectors on the LOR. According to the equation (2.4), the rate of random events increases proportionally with the width of the coincidence timing window. Thus, the amount of random events can be decreased by using faster electronics and shorter time window. Another factor affecting the rate of randoms along the LOR is the number of occurred single events among it, which in turn depends on the amount of administered activity to the subject. In other words, increase in activity results in larger amount of random events along the LOR [3].

The most common method used for random correction is *delayed window method*. This approach uses in addition to the normal coincidence window a delayed window, which is delayed by a time that is much greater than its width [18]. For instance, if the width of the coincidence window is 12 ns (1-12), the delayed window duration is 64-76 ns. Thus, with this time delay only events that have time difference between 64 to 76 ns are accepted. In other words, only random events are detected in the delayed window as the photons in true and scatter coincidences hit the detectors within a few nanoseconds. On the other hand, in the normal window all prompt events (true + scatter + random) are detected. Therefore, by subtracting the number of detected random events from the total number of prompts, the amount of true coincidences in addition to the scatter coincidences for a detector pair can be estimated. Consequently, the resulted data which contains true and scatter coincidences can be corrected using a proper scatter correction method.

Scatter correction

Scatter correction becomes more significant with evolution from 2D mode acquisition to 3D, as the scatter fraction increases from 15% in 2D mode to more than 40% in 3D mode in modern PET scanners [3]. Scatter correction is the most difficult correction necessary in PET, because a scattered event can be only distinguished from a true event on the basis of the energy [13]. Since scatter involves a loss in the energy of the photon, using a narrower acceptance energy window, the number of scattered events can be reduced. However, narrowing the energy window will result in smaller amount of true events as well. Thus, additional scatter correction techniques are required. These methods are mainly divided into three categories as analytical, dual energy windows and simulation based methods [13].

A simple way for scatter correction is to fit an analytical function to the smearing of radioactivity occurring outside the object in the sinogram. This method is based on the facts that all coincidences recorded outside the object are due to scatter and the scatter distribution contains mainly low spatial frequencies. The method is computationally efficient and simple to implement. However, its drawback is that the scatter distribution is not always estimated properly with a smooth analytical function, especially in thorax where tissue density is miscellaneous leading to over- or under- subtraction. [9]

In dual energy window approach coincidences are divided in two groups of different energy windows, for example, 250-399 keV and 400-600 keV. It is assumed that the lower window contains only scattered photons while, the upper window contains both scattered and unscattered photons. For scatter correction some fraction of the low energy window counts are subtracted from the high energy window counts. However, as energy resolution of the detectors is limited, both windows contain scattered and unscattered events. Furthermore, the low energy window also contains multiple scattered photons, which have a different spatial distribution than the single scattered events. These reasons lead to difficulties in utilization of the dual energy window technique. This method also involves determination of a number of calibration constants to consider efficiency differences in the two windows and to define the fraction of the low energy window which should be subtracted. Since determination of these constants is dependent to the object size, this approach is used in applications where the object geometry is precise and remains constant during the study. [13]

The most accurate scatter correction methods are simulation based approaches. These methods use a transmission scan in addition to the emission scan to determine the attenuation map of the object. First the scatter is estimated by reconstructing emission data without scatter correction. Consequently, using these images as the initial estimate of the source distribution as well as the resulted attenuation map of the object from the transmission scan, the scatter is simulated either using a single scatter model, an approximate analytical model or using a Monte Carlo simulation. Simulation based techniques are more time consuming compared to the other techniques as they involve additional image reconstructions and computationally expensive simulations. [13]

Dead time correction

Dead time of the PET system is defined as the process time required for it to detect an event. Thus, the system is unable to detect another event during this time. As PET device is composed of different detectors with different efficiencies, the efficiency of each detector block such as decay time of the scintillation crystals and time to integrate charge from PMTs (integration time) affect the dead time of the whole system.

Dead time correction is accomplished by empirical measurements of observed count rates due to amount of administered activity. Using these data, the dead time loss is calculated and compensated in the measured data. Moreover, in order to improve the dead time correction other techniques including use of buffers where the overlapping events

are held during the dead time, using pulse pile up rejection circuits and use of high speed electronics can be applied [3].

Attenuation correction

Attenuation is defined as the energy loss of the photons due to their interaction with the surrounding tissue. It results in non-uniformities in the images due to the loss of more coincidence events from the central tissues with respect to the peripheral tissues of an organ. In addition, two photons may traverse different organs along the LOR leading to non-uniformities in the image as well. [3]

When the annihilation photons travel towards the detectors, they traverse different thicknesses inside the body. If μ is linear attenuation coefficient for 511 keV in the tissue, a and b are the distances traversed by the photon pair, and D is the total thickness of the subject (see Figure 2.10), the probability of a coincidence detection is calculated by equation (2.6):

$$P = e^{-\mu(a+b)} = e^{-\mu D}, \tag{2.6}$$

In equation (2.6) is assumed that total tissue travelled by the photons has the same attenuation coefficient, while they travel different tissue and organs inside the body. So the equation (2.6) becomes:

$$P = e^{-\sum_{i=0}^{n} \mu_i D_i}, \tag{2.7}$$

where μ_i and D_i are the linear attenuation coefficient and thickness of i:th organ or tissue and n is the number of organs or tissues the photon travels through. The main purpose of such method is to find a map of linear attenuation coefficients (μ-map) for every point within the object, which are applied to the dataset after the acquisition.

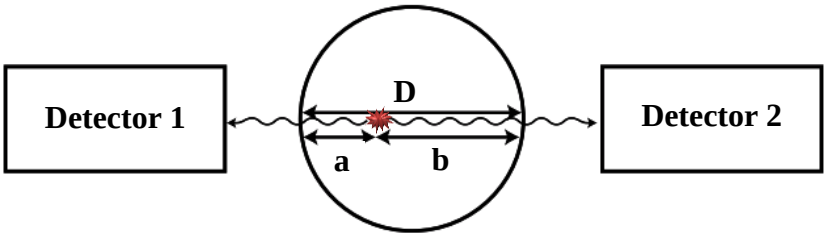

Figure 2.10. *Two photons are detected by detectors after traversing different distances a and b inside the subject. D is the total thickness of the subject. Adapted from [3].*

Attenuation coefficients can be measured with a source outside the body such as a CT scan. For example in the modern PET/CT dual scanners the collected CT data are

used for calculating the attenuation coefficients in the body. The estimated attenuation coefficients are then used for attenuation correction of the PET data [7].

3 AXIAL PET

As discussed before, PET imaging has an important role in cancer diagnosis. However, the performance of PET in the studies of specific organs such as breast, prostate, brain as well as in the small animal studies is limited. The main factors affecting the performance of the scanner are its spatial resolution and sensitivity, although many years of research and development have been focused on improvement of these features of the PET scanner.

In the standard PET camera, scintillator crystals are arranged radially around the patient and readout from one end by the photodetectors. This geometry for the crystals does not allow achieving the depth of interaction, which causes the parallax error and results in degradation of spatial resolution. Moreover, it leads to the non-uniform spatial resolution over the FOV, because the spatial resolution worsens as distance of the event detection from the center of FOV increases (see subsection 2.4). One way to reduce this error is to use crystals of shorter size. However, reducing the size of the crystals leads to a lower sensitivity in the system as well. Therefore, a new design is required in order to avoid the compromise between spatial resolution and sensitivity.

In 1988, Shimizu et al. proposed a new geometry for the scanner, where scintillator crystals were aligned axially around the subject and a matrix of crystals was readout on both sides by segmented photodetectors [19]. This way, the axial coordinate was derived from the light levels detected at the two ends of the crystal. A subgroup from this article worked several years on the implementation of a similar scanner where double side readout was accomplished by Hybrid Photon Detectors (HPD). However, an axial resolution in the millimeter range could not be achieved.

In a new implementation of the axial concept, a good axial resolution is achieved by employing WLS strips aligned orthogonal to the crystals. Both crystals and WLS strips are readout individually by fast Geiger-mode Avalanche Photodiodes (G-APDs) from Hamamatsu, marketed as Multi Pixel Photon Counters (MPPC). This new implementation of PET is explained in detail in this chapter.

3.1 The AX-PET concept

In the novel Axial PET design, crystal bars are stacked in several layers aligned in parallel with the axis of the scanner (Z-axis) (see Figure 3.1 (a)). The scintillating crystals ("LYSO", $Lu_{1.8}Y_{0.2}$- SiO5:Ce) have the desired properties such as high density, high light output, short decay time, and excellent energy resolution [20]. The layers of crystal are interleaved with an array of WLS strips, placed orthogonal to the crystals. The WLS strips are of type EJ-280-10x from Eljen Technology [6]. Both crystals and WLS strips

are readout by MPPCs at one end, while the other end is covered by a thin reflective Aluminum coating.

When a photon deposits its energy in the crystal, a correlated amount of light is emitted isotropically. As shown in Figure 3.1 (b), the light emitted inside the cone of the total reflection is captured by the MPPC, while a fraction of light which are emitted outside the cone, are absorbed by a WLS strip or several strips aligned under the crystal. The WLS strips convert the wavelength of the photoelectrons (from ~420 nm to ~490 nm), after which a fraction of them are captured by the MPPCs connected to the WLS strips [6]. The energy levels captured by the MPPCs, attached to the crystals and WLS strips determine the 3D coordinate of the photon interaction point.

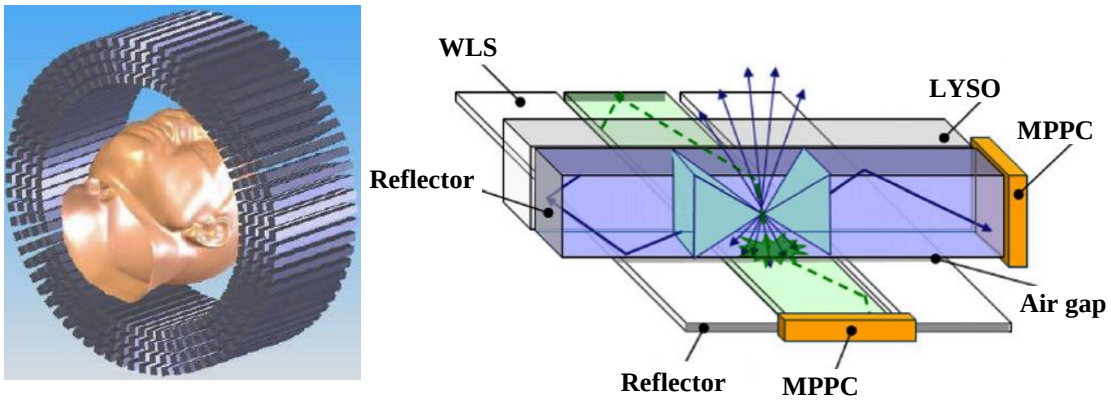

Figure 3.1. *AX-PET scanner design. (a) Arrangement of the crystals around the patient [21]. (b) Principle of the light propagation in a crystal and underneath WLS strip [6]. When a photon strikes a crystal, the crystal emits scintillating photons such that part of the photons penetrate the crystal and are absorbed by the underneath WLS strip/strips.*

The signals collected from the LYSO crystals define the X and Y coordinates of the interaction point and the signals from the WLS strips determine the axial coordinate i.e. Z-coordinate of the hit (see Figure 3.2). Therefore, in order to define the X and Y coordinates of the hit, the hit crystal is identified and the X and Y coordinates of the center point of it are assigned as corresponding coordinates of the interaction point. As Figure 3.2 shows, when a photon hits a crystal, in most cases, more than one WLS strip detect a signal above the threshold. In order to identify one WLS strip, which determines the Z coordinate of the interaction point, a technique called as center of gravity (CoG) has been applied to the group of WLS strips above the threshold [22].

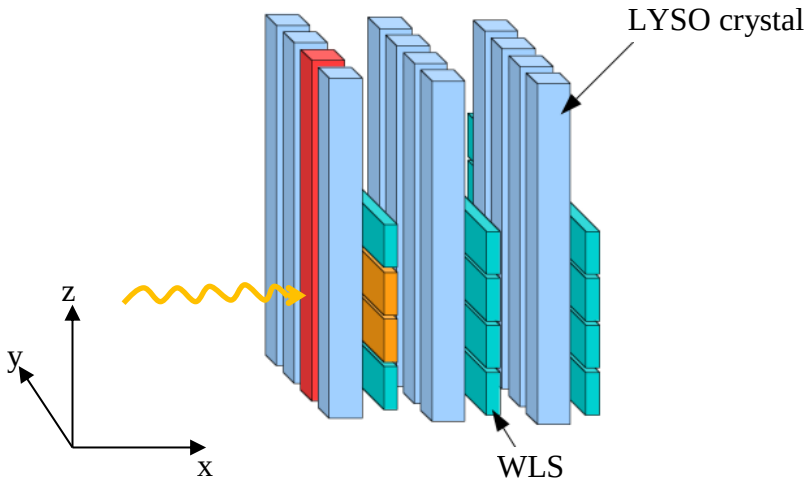

Figure 3.2. *Illustration of the 3D coordinates determination using the hit crystal and the corresponding WLS strips. The hit crystal (shown in red) defines the X and Y coordinates of the interaction point and the WLS strips with a signal above threshold (shown in yellow) determine the Z coordinate of the interaction point. Adopted from [23].*

Before applying the CoG method, in order to remove the contribution of the noise, a clustering algorithm is employed on the WLS strips placed on the same layer. As illustrated in Figure 3.3, a cluster is defined as a group of adjacent WLS strips, which detect a signal above the threshold (200 keV). This way, only clusters are considered in calculation of the Z-coordinate of the hit resulting in more accurate axial coordinate.

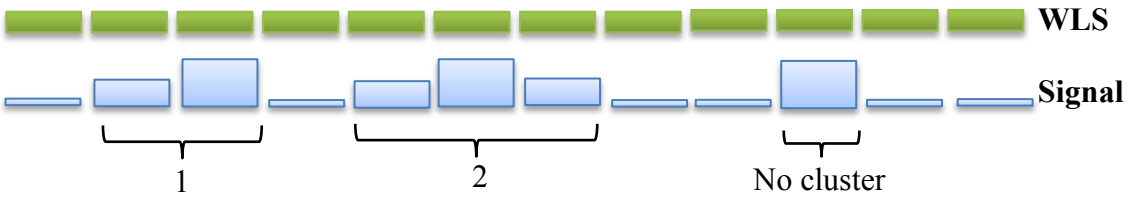

Figure 3.3. *The process of clustering of the WLS strips with signals above the threshold. Here two clusters of sizes two and three are found.*

Once all clusters in a layer are defined, the biggest cluster is selected for applying the CoG method. A CoG method utilizes the value of the signals in the WLS strips and the coordinates of the center point of the WLS strips to define the point of interaction. I.e. Z-coordinate of the interaction point is calculated using equation (3.1):

$$Z = \frac{\sum_{i=1}^{n} v_i z_i}{\sum_{i=1}^{n} v_i}, \tag{3.1}$$

where Z represents the defined Z coordinate of the interaction point, v_i indicates the values of the collected signals from the WLS strips in the cluster, and Z_i is Z-coordinate of the corresponding WLS strips.

3.2 Development steps in AX-PET

The first AX-PET scanner prototype consisting of two modules were made at CERN (European Organization for Nuclear Research) in 2009 [5]. Each module of this demonstrator contains six layers of scintillator crystals each one containing eight crystal bars. The crystal layers are interleaved with a layer of 26 WLS strips. Both crystals and WLS strips are read individually by MPPCs. In this work, each module of the demonstrator was characterized individually using a ^{22}Na point-like radioactive source (activity 925 kBq, diameter 250 μm) and two tagging LYSO crystals of different size, which were readout by fast PMTs [5].

Later in 2009-2010 the spatial resolution of the images obtained by the demonstrator was studied [24]. For this purpose, two modules were set in coincidence at a distance of 150 mm and ^{22}Na point-like source was placed on a rotating table at different positions of the FOV. The resolution on the transaxial plane (x, y) was calculated with the equation $\sigma_{x,y} = d/\sqrt{12}$, where d represents the transverse dimension of the crystal bars. Thus, with the crystal bars of size 3×3 mm^2, the resulting resolution was $\sigma_{x,y}$ = 0.87 mm. The final resolution in the axial dimension was σ_z = 0.64 mm, once the effect of positron range and finite size of the source were subtracted. Subsequently, a set of tomography images were reconstructed using a reconstruction algorithm based on Maximum Likelihood Expectation Maximization (MLEM) method. The demonstrator was also tested by measuring different phantoms, fitting the size of the field of view. As a result, the resolution of at least 2 mm in all three dimensions was defined [24].

Although the rotation of the phantoms placed on the rotating table between the two fixed modules allows for tomographic imaging, it also results in a small transaxial FOV. Therefore, a new gantry set up was developed [22]. In the new design one module of the demonstrator was fixed, while the other was rotated during the acquisition (see Figure 3.4). This lead to a larger FOV and allowed for characterization of more complex structures. The new gantry design was tested with phantoms filled with ^{18}F radiotracers and small animals (mouse and rat) as well.

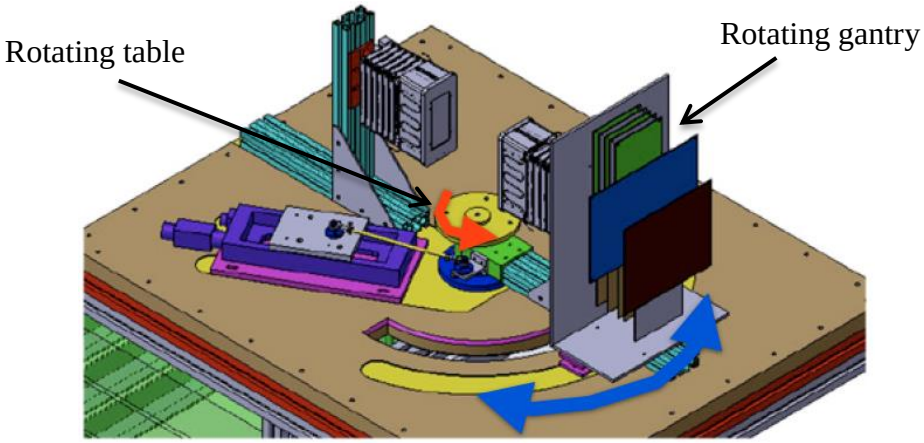

Figure 3.4. *Rotating gantry setup for the Ax-PET demonstrator. The gantry and rotating table are mounted to ensure an extended FOV [21].*

Recently, the use of Digital Silicon Photomultipliers (dSiPM) instead of the G-APDs in AX-PET was studied and preliminary tests were accomplished [26]. As described in Section 2.5, the time resolution of the system limits the detection of the annihilation point in TOF PET. The new photodetectors are a fully digital implementation of G-APDs with a capability of recording the timestamp with a very good intrinsic time resolution. This feature of the dSiPMs makes them suitable for TOF PET. Thus, the SNR ratio can be improved significantly in a TOF image.

3.3 Advantages of AX-PET

The AX-PET concept allows the 3D reconstruction of the interaction point of the photon with the crystals for both the photoelectric and Compton interactions. Therefore, the parallax error due to absence of DOI information appeared in the conventional PET scanners can be overcome.

The sensitivity of such scanner can be increased simply by adding number of crystal layers in the scanner. Moreover, as with the new design part of the Compton scatter events occurred between the crystals (inter crystal scatter, ICS) are detected and included in the image reconstruction, it increases the sensitivity [25].

The spatial resolution of the scanner can be adjusted without compromising the sensitivity by tuning the transverse size of the crystals (resolution in x and y directions) and width of the WLS strips (resolution in z direction). In other words, the smaller the size of the crystals the better resolution in transaxial direction as well as the smaller the width of the WLS strips the better resolution in axial direction is obtained.

Moreover, use of the solid state G-APDs makes the scanner insensitive to magnetic fields, allowing the combination of PET and MRI [5].

4 AVANTOMOGRAPHY DEMONSTRATOR

As described in previous chapter, the most desirable feature of the AX-PET concept is that it allows improving spatial resolution and sensitivity independently. Therefore, very sensitive small scanners with good spatial resolution capability can be produced. Such scanners are used for preclinical studies as well as in clinical studies where a certain part of the body is imaged (brain, breast, prostate).

Based on the AX-PET concept a new small demonstrator called as AvanTomography was built in Tampere University of Technology. In this demonstrator, the data is recorded as single events during the acquisition and the coincidence events are determined after the acquisition using dedicated programs. This way, dead time of the system is decreased comparing to the AX-PET project at CERN, where coincidence events were defined using trigger electronics during the acquisition [6]. Decreasing of the dead time results in improved time resolution allowing a smaller coincidence window, thus suppressing the random events in the AvanTomography demonstrator. In addition, this scanner provides timing information on individual channels, which leads to the better time resolution compared to the AX-PET project at CERN, where the timing measurements on the outputs of the modules based on summed signals were performed using an oscilloscope [6].

The AvanTomography demonstrator contains four similar modules forming a rectangular shape for the scanner. Figure 4.1 shows arrangement of the modules in this scanner. Although this prototype is made of only four modules, it allows for adding more modules in axial direction or in transaxial direction. Additional layers in axial direction result in larger FOV, while adding them in transaxial direction leads to higher stopping power of detectors, and thus increasing the sensitivity. This chapter describes the constituent components and functionality of this new AX-PET prototype.

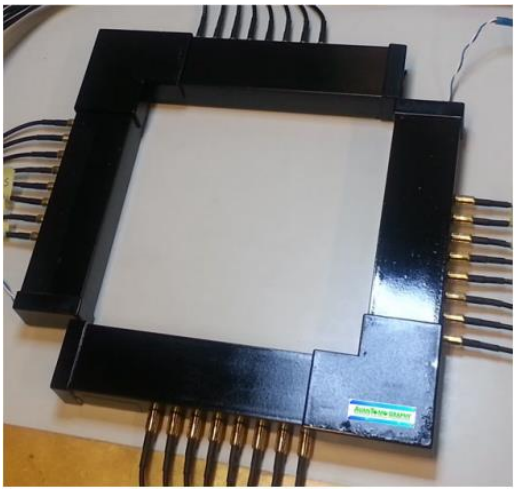

Figure 4.1. *The AvanTomgraphy demonstrator is made of four identical modules, constructing a rectangular shape [28].*

4.1 Components of a single module

Each module of the demonstrator contains two layers of LYSO crystals. The first layer of crystals contains three crystal bars, while the second layer contains only two crystals. The LYSO crystals used in this prototype are 150 mm long with cross section of 3×3 mm^2. In the second layer the crystals are staggered from the first layer by half the crystal pitch (1.75 mm). The crystal pitch (distance between centers of the two adjacent crystals) in a layer is 3.5 mm. In order to hold crystals in place and shield them from external light, they are located inside a non-conductive and non-transparent plastic container. The two layers are also optically isolated by this material [28].

A layer of forty three WLS strips is mounted above each crystal layer with an air gap of 0.2 mm. The WLS strips have the dimensions 15×3×1 mm^3 and are placed orthogonal to the LYSO crystals as shown in Figure 4.2.

One end of the crystals and WLS strips is attached to the MPPCs of active area of 3×3 mm^2. They are attached with an optically clear adhesive with light transmission of ~99% [28]. In order to reflect the photons reaching to the other end of the crystals and WLS strips, it is covered by a thin reflective aluminum coating. Moreover, a thin foil of dark plastic is placed between the adjacent MPPCs in order to avoid electrical conduction and propagation of the light between them. Figure 4.2 illustrates arrangement of the main components inside a module.

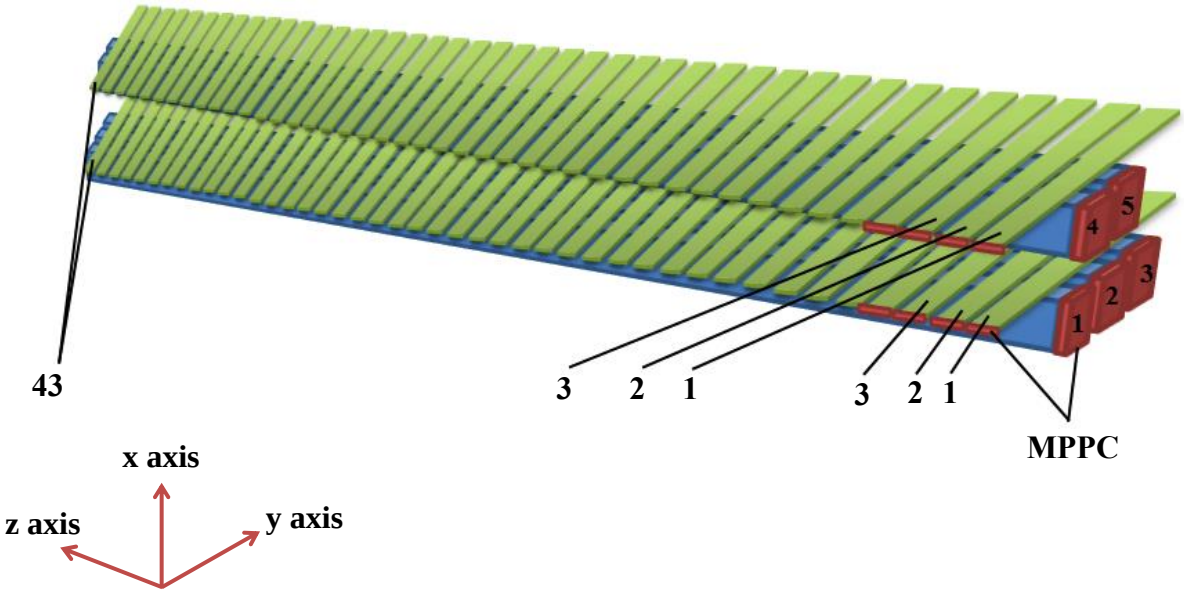

Figure 4.2. *Assembly of the crystal bars and WLS strips inside a single module of the AvanTomography demonstrator. In addition, the defined labels for the crystals and WLS strips as well as the determined coordinate system inside the modules are illustrated.*

Determination of the crystals and WLS strips IDs

The crystals and WLS strips inside each module must have an ID for accurate identification. A numbering system starting from 1 is used for this purpose. As shown in Figure 4.2 numbering of the crystals starts from the first crystal layer and continues to the next layer. Another issue which is taken into account while numbering the crystals on a layer is the side at which the above WLS layer is attached to the MPPCs. I.e. in a crystal layer, the crystal which is near to this side has smaller value than the one positioned further.

The WLS strips are numbered in the same way as the crystals, but here the numbering of two layers is done independently. Thus, WLS strips at each layer have IDs in 1-43 range. Enumeration of the WLS strips in a layer starts from the nearest WLS strip to the side at which the below crystals are attached to the MPPCs (see Figure 4.2).

The selected IDs for the crystals and WLS strips are used to determine the direction of the Y and Z-coordinates inside the module such that direction of Y-coordinate is according to the increment of the LYSO numbers in a layer. In the same way direction of the Z-coordinate is defined using the WLS IDs in a layer (see Figure 4.2). Furthermore, the X-coordinate inside the module starts from the first crystal layer and continues to the next layer as shown in Figure 4.2.

4.2 Determination of module IDs

The label used to identify the modules of the scanner contains 3 parameters. Since the scanner is made of four modules, the first parameter has a range of 1-4. As shown in

Figure 4.3, the module with the same Z-axis as the scanner (in the same direction), obtains the value *1* as its first parameter. The value of this parameter increases in clockwise direction in other modules.

As mentioned before, this demonstrator has a flexible size such that additional module layers can be constructed above the current modules or beside them in the future. The second parameter of the module label is used to define its layer in Y-axis of the scanner. As current design of the scanner contains only one layer in mentioned direction, this parameter is set as *1* for all existent modules. The last parameter is used for additional layers besides the current modules so that the inner modules have the value *1*, and it is increased in outward direction.

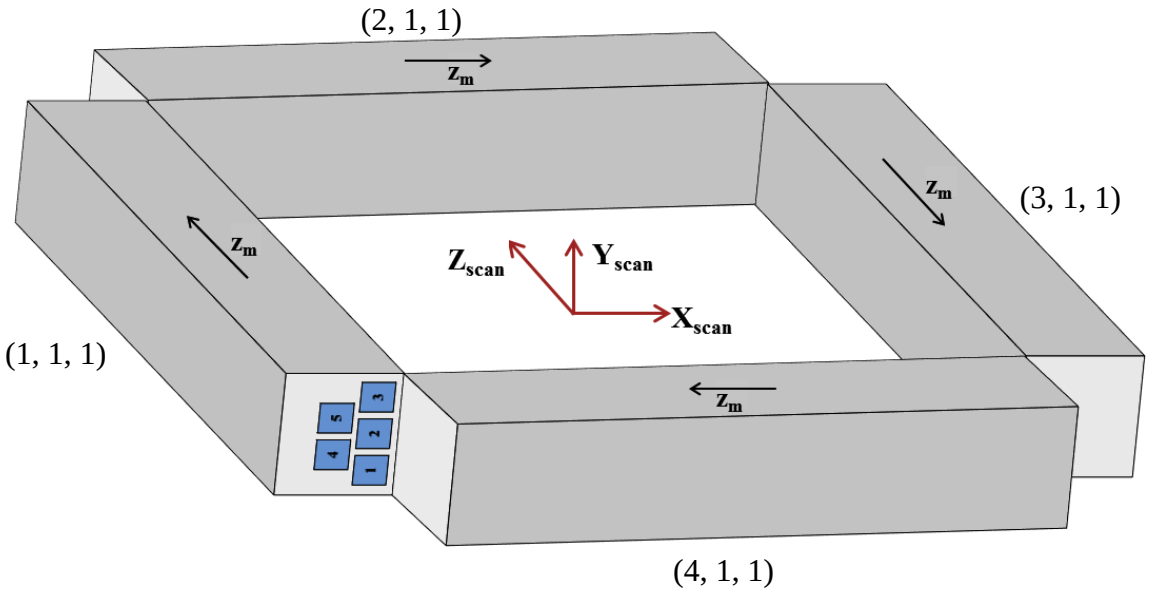

Figure 4.3. *Determination of the module IDs. The module with the same Z-coordinate as the scanner Z-coordinate has value "1" as the first parameter of its ID and value of this parameter is increased in clockwise direction in other modules. The scanner 3D coordinates are shown with subscript "scan" and the Z-coordinate inside the modules is represented with the subscript "m". In order to clarify the crystals assembly in the scanner, their set up is shown for the module (1, 1, 1).*

4.3 Data acquisition

The AvanTomography demonstrator provides analogue readout for all crystals and WLS strips. Each module of the demonstrator contains 86 WLS strips (43 WLS strips at each layer) and 5 crystals, resulting in 91 different channels. Thus, for four modules 91×4=364 channels are provided. All the channels are processed in parallel. The charge levels obtained from each channel are converted from analogue to digital value (ADC), after which the charge units (pC) are converted into energy scale (keV).

In order to convert the charge signals to energy scales, first each channel must be energy calibrated. The purpose of energy calibration is to equalize all the channels and

also to correct the MPPC response, which is not perfectly linear. In a previous work by Tiziana Zedda [28], the energy calibration for one LYSO crystal was performed and the equation 4.1 was derived for the conversion from charge to energy scale, where Q represents the charge signal (pC) and E indicates the corresponding signal in energy scale (keV). The parameters a_1, b_1, and c_1 are evaluated in [28] as -327.154, -8.869×10^{-4} and 326.3476 respectively.

$$E = \frac{1}{b_1} log_e\left(\frac{Q - c_1}{a_1}\right) \tag{4.1}$$

Individual energy calibration is necessary for all channels. Consequently, for every channel the equation of charge to energy conversion can be determined. When charge signals are converted into energy scales, energy levels of the signals coming from LYSO crystals are assessed and signals, which fall into the threshold levels, say 100-1024 keV are assigned as an event. The selected threshold values should be such that the noise as well as high energy signals, which do not contain useful information for coincidence events are rejected.

Each event word holds information on the time of the event detection, energy of the signal, module and LYSO IDs, and the corresponding WLS strip layer. The time of the event detection is used afterwards for finding the events in the same time window. The module and LYSO IDs of the event indicate in which module and in which LYSO crystal, the photon is detected. The WLS strip layer of the event is selected according to the defined LYSO for the event. I.e. in case the event is detected in LYSOs with label 001, 010 or 011 (1, 2, or 3), the first WLS strip layer is saved for the corresponding event and if the label of the LYSO is 100 or 101 (4 or 5), the second WLS strip layer is recorded in the event word. The constructed words of the detected events are transferred to the PC for coincidence detection and further processing. Figure 4.4 shows different steps executed from data acquisition to the image reconstruction.

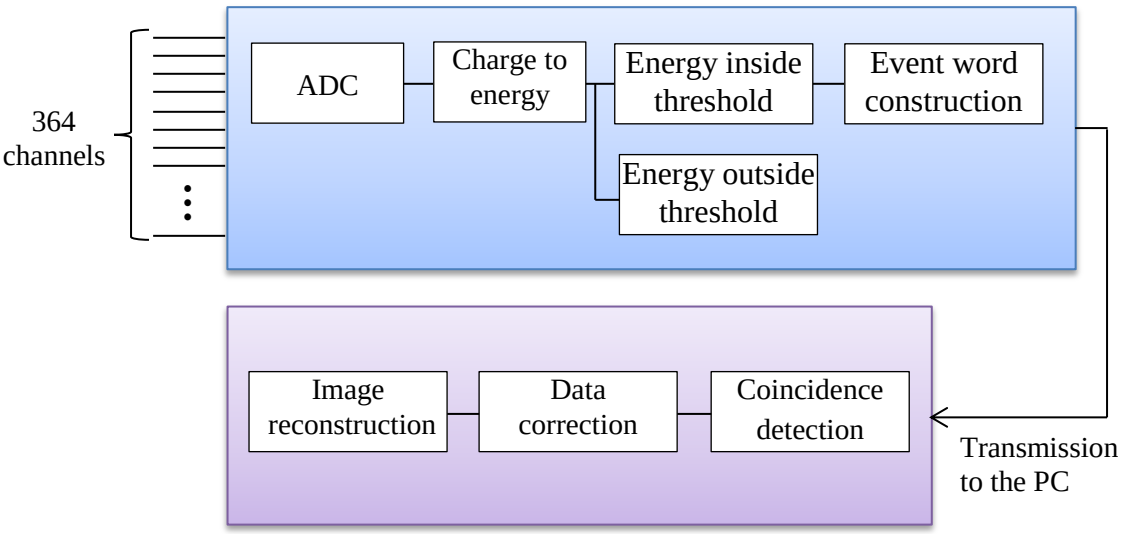

Figure 4.4. *Illustration of different sections of the system. Collected analogue signals from crystals and WLS strips are first converted to digital signals. The charge signals are then converted to energy scales. The energy value of the signals coming from the crystals defines the event construction i.e. they define whether the signal is considered as an event. The set of event words are transmitted to the PC for detection of coincidence events. After the coincidence detection, proper correction methods are applied to the data. Using the corrected data, the PET image is reconstructed.*

We can calculate the data stream to the PC by determination of the amount of detected events in time unit as well as the length of each event word. As described before, a single event word contains five fields. Below is described how the required space for recording each such field is calculated.

Time stamp: If the system has a time resolution of 0.5 ns and the time stamp of the system is reset in every second, 2×10^9 different states are resulted for the time stamps of the events. As using 31 bits, 2.147483648×10^9 different states can be saved; this amount is selected for recording the time of the event detection.

Energy: The minimum energy value for an event is 100 keV as the events with smaller energy value are discarded. The maximum value can be assumed as 1024 keV (detection of two photons at the same time). So a length of 10 bits is defined for saving energy in the mentioned range.

Module: Label of the modules contains three fields, where the first field has a range in 1-4. We can also assume a range of 1-4 for the next fields in order to allow the construction of three additional module layers above the current modules or besides them. So by reserving 2 bits for each field, a number of 6 bits is reserved for saving the module label.

LYSO: Each module contains 5 LYSO crystals. Since using 3 bits 8 possible numbers can be saved, this amount of bits is enough for storing the LYSO labels (1-5).

WLS strips: As mentioned before, there is a layer of 43 WLS strips above each crystal layer and for each crystal, only corresponding layer of WLS strips is considered. One way to save the WLS strips data is to reserve 43 bits where a "1" represents a fired WLS strip and a "0" represents a non-fired WLS strip. This way, only the ones with energy level above the threshold are assumed to be fired. We can reserve more space for each WLS strip in order to record the energy value of it as well. In this case, by reserving 10 bits for each WLS strip, a number of 430 bits is used for saving the energy of the WLS strips of an event.

Table 4.1. *Definition of the length of an event word. (a) One bit is reserved for each WLS strip of the event, (b) 10 bits is reserved for each WLS strip.*

(a)

Bit	Field
0-30	Time stamp
31-40	Energy
41-46	Module
47-49	LYSO
50-92	WLS strips

(b)

Bit	Field
0-30	Time stamp
31-40	Energy
41-46	Module
47-49	LYSO
50-479	WLS strips

Tables 4.1 (a) and (b) illustrate the number of bits used for recording each field of an event word, where in case (a), 43 bits are reserved for the WLS strips resulting in 93 bits required to save an event. In case (b), 430 bits is assumed for the WLS strips of the event, thus a length of 480 bits for each event is resulted. For determining data stream to the PC, we need also to know the amount of detected events per second, which depends on the total stopping mass in the scanner.

In order to estimate the amount of events arisen by the total stopping mass in the scanner, we can utilize the number of counts and stopping mass of High Resolution Research Tomograph (HRRT) scanner. This scanner contains in total 119808 crystals of size 2.15×2.15×10 mm^3 resulting in ~5.54 Mmm^3 stopping mass [7]. While a total of ~2.6 Mevents are detected in a second, 1 mm^3 stopping mass corresponds to ~0.47 events/sec. The AvanTomography demonstrator contains 20 crystals consequent to 20×3×3×150 = 27 kmm^3 mass. Using the amount of events corresponding to a correlative stopping mass in the HRRT scanner, ~12.7 kevents/sec is accounted for the AvanTomography scanner.

Finally, we can determine the amount of data stream in both cases presented in tables 4.1 (a) and (b). Table 4.2 shows the calculated data stream for both cases. The columns 1-4 represent the amount of bits used for recording the WLS strips data of an

event, the number of bits resulted for an event, the calculated amount of events detected in a second and the accounted amount of data stream in a second in the AvanTomography demonstrator.

Table 4.2. *Illustration of the calculated values in order to determine the data stream transferred to the PC.*

Bits per WLS strip layer	Bits per event	Events per second	Bits per second
43	93	12700	1181100
430	480	12700	6096000

Considering the Figure 4.4, this thesis concentrates on the event word construction and the coincidence detection sections, which involve smaller steps illustrated in Figure 4.5. The constructed event words are first classified in three groups of high, desired and low energy events after which the events in the desired energy window are selected for coincidence detection. The high energy and low energy events are used for data corrections afterwards. When the coincidence events are determined, using the methods given in next chapter, their 3D position in the scanner is calculated. Positioned coincidence events constitute the raw data saved for further processing.

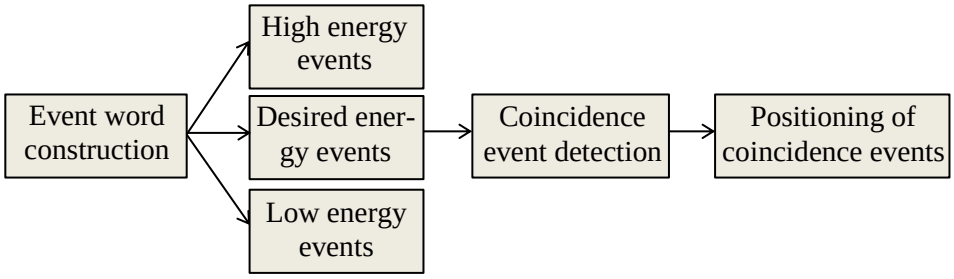

Figure 4.5. *Illustration of different steps covered in this thesis.*

5 POSITIONING OF COINCIDENCE EVENTS FOR AVANTOMOGRAPHY DEMONSTRATOR

This chapter presents the approaches employed on the acquired data in order to determine the coincidence events as well as to define 3D location of the coincidence events. For this purpose, first a coincidence window of a reasonable length is selected and then using this window the coincidence events are determined. Consequently, in order to define the location of the resulted coincidence events, first their position inside the modules (location of the hit with respect to the module center i.e. intramodular hit location) is defined and then it is converted to the scanner coordinate system (location of the hit with respect to the scanner center i.e. intermodular hit location). All the methods presented here are implemented by the MATLAB program.

5.1 Coincidence window definition

The length of the coincidence window is important parameter determining the amount of random events, the smaller the coincidence window the less the amount of random events. However, as discussed in Section 2.3, minimum length of the coincidence window is limited by the distance between the detectors. Thus, we can calculate the minimum length of this window taking into account the distance of the detectors in the scanner.

The time difference between the detection of annihilation photons can be calculated using equation 5.1, where x_1 and x_2 represent the distances traveled by each annihilation photon, c indicates the speed of light (30 cm/ns) and d is distance of the annihilation point from the midpoint of the corresponding LOR. Figure 5.1 (a) illustrates different parameters set in this equation.

$$\Delta t = \frac{x_1 - x_2}{c} = \frac{\left(\frac{LOR}{2} + d\right) - \left(\frac{LOR}{2} - d\right)}{c} = \frac{2d}{c}\, ns \tag{5.1}$$

According to the equation (5.1), the time difference between the detection of the photons increases with the parameter d. I.e. when $d = 0$ (annihilation occurs at the midpoint of the LOR) Δt is zero as well. Similarly, Δt is at maximum when d is at maximum. From Figure 5.1 (a), can be observed that the parameter d in case of having the largest value (annihilation occurs next to the modules), equals to $LOR/2$. Although such annihilations may occur only when the FOV fits the scanner whole area, but as the size of the FOV is not defined, we assume the biggest possible size for the FOV here.

As length of the LORs is different for the occurred annihilations at different sites of the scanner, the parameter *d* gets the maximum value when annihilation produces the longest LOR. This is illustrated in Figure 5.1(b). The length of *d* for this case can be determined using the Pythagorean Theorem:

$$d^2 = (7.5cm)^2 + (7.5cm)^2 \quad \Leftrightarrow \quad d = \sim 11cm \tag{5.2}$$

Using the equations (5.1) and (5.2) the maximum difference time in detection of the two photons can be calculated as $\Delta t = \sim 0.73$ ns. The length of the coincidence window is defined as $\tau = 2 \times \Delta t$, because in order to find the coincidence event of a single event, Δt ns before as well as after the detection time of the photon must be investigated. Therefore, the length of the coincidence window for this demonstrator can be set as 1.5 ns. However, as mentioned before, the timing resolution of the system is limited and may result in larger detection time window of the coincidence events. In order to take into account the effect of the time resolution, a window of length $\tau = 3$ ns is used for this work.

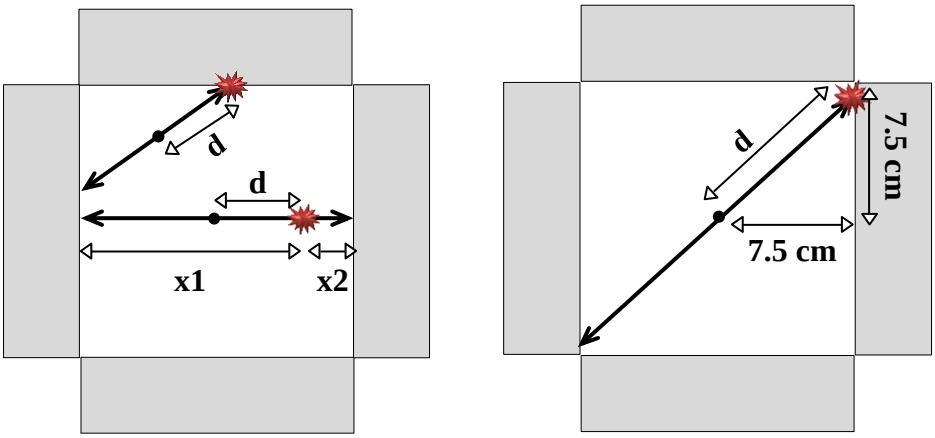

(a) (b)

Figure 5.1. *(a) Illustration of parameters set in equation (5.1). Parameter d represents the distance of annihilation point to the midpoint of the LOR, x1 shows the distance traveled by one of the photon pair before the detection and x2 is the distance traveled by the other photon. (b) Illustration of the annihilation, which produces the longest LOR in the scanner. Since length of the modules is 15 cm, distance of each module to the scanner center is 7.5 cm.*

5.2 Data categorization

Detected events are stored as a list of single event words, where each event contains five fields explained in Section 4.3. The stored events have different energy values including energies smaller or bigger than the energy resulted in a photon interaction (511 keV). Different reasons may lead to production of such events including Compton scatter or

interaction of two single photons at the same time (2 × 511 keV = 1022 keV). Since we are interested in detection of 511 kev photons, events are classified into three groups of low, desired and high energy events. The low energy events have energy values between 100-399 keV, which will be used afterwards for the scatter correction. The desired events have the energy in the range of 400-600 keV. Finally, the events with higher energy than 600 keV are stored separately as high energy evens (these events may be used for further data corrections). As 511 keV events fall into the group having energy in 400-600 keV range, the events in this class are selected to process and to search the coincidence events.

Table 5.1 illustrates the range of different fields of the single events selected for coincidence detection. These events are arranged according to their time stamp in growing order. The label of the module contains three fields as explained in subsection 4.2. Each such field has a range of 1-4. A vector of WLS strips consists of a series of "0" (indicates a non-fired WLS strip) and "1" (indicates a fired WLS strip) with a length of 43.

Table 5.1. *Illustration of the range of the fields existing in a single event.*

Range	Field
0-10^9 ns	Time stamp
400-600 (keV)	Energy
1-4	Module ID
1-5	LYSO ID
0-1	vector of WLS strips

5.3 Axial coordinate determination

The data stored in the WLS strip vector of the event is used to determine the axial coordinates. The procedure of defining Z-coordinate is as follows. First all clusters having the value "1" are selected. Consequently, the CoG method is applied on the biggest cluster found in the group of clusters. Since all WLS strips in a cluster have the same value ("1"), the task of such method is to determine the ID of the WLS strip at the center of the cluster. Therefore, if the length of the cluster is odd, one WLS strip is selected as the interaction point. On the other hand, if the cluster has even size, two WLS strips in the middle of the cluster are selected in order to define the center point among them as the Z-coordinate of the interaction. The third possible case is existence of two clusters which have the same sizes. As axial coordinate of such event cannot be defined, these singles are rejected before coincidence detection. Figure 5.2 illustrates all three cases as well as the process of the used CoG method.

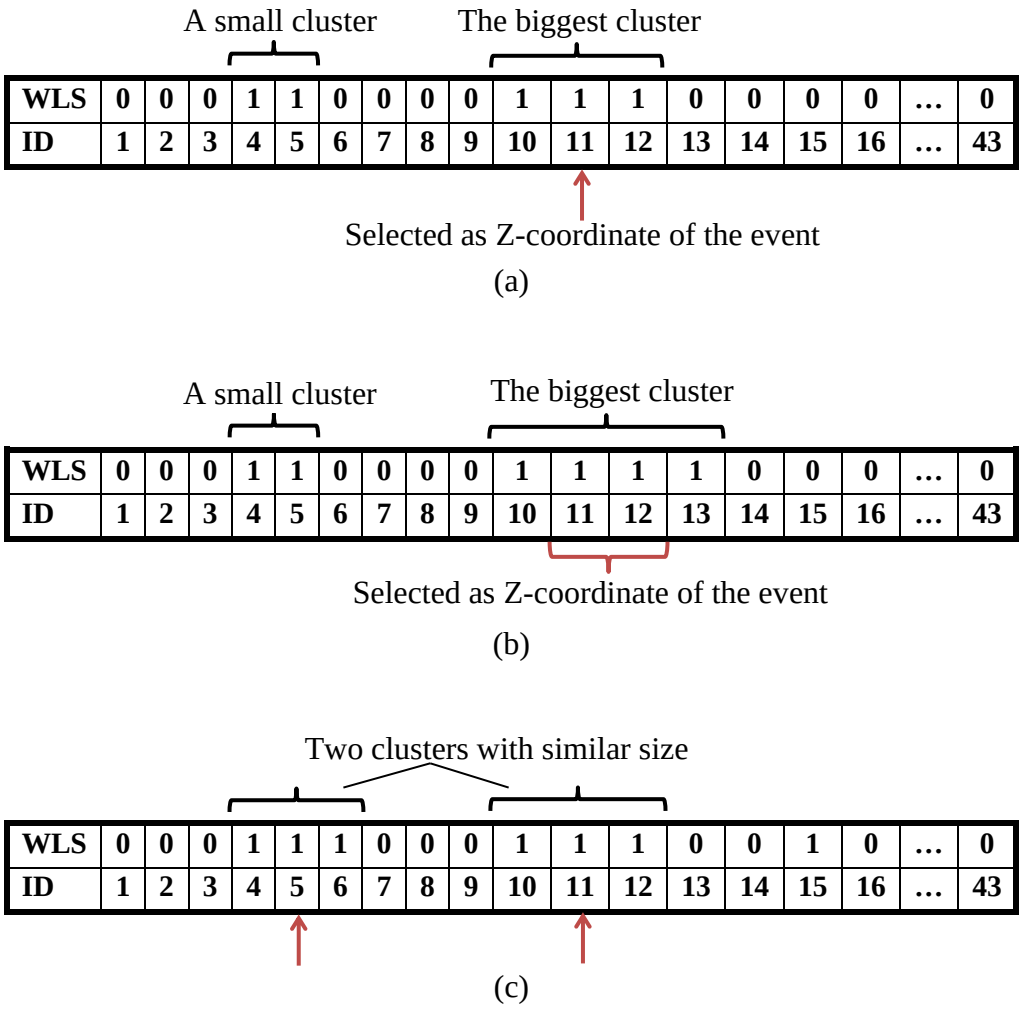

Figure 5.2. *Illustration of the process of axial coordinate determination for the interaction point. (a) In this case the size of the biggest cluster is odd and the WLS strip located at the center of the cluster is assigned as the Z-coordinate. (b) The size of the biggest cluster is even and two WLS strips at the middle of the cluster are chosen as Z-coordinate. (c) Two biggest clusters of the same sizes are found, thus the axial coordinate cannot be defined.*

5.4 Coincidence detection

As discussed in Chapter 2, the true counts are the events detected in predefined time window. However, as photon pair travel on opposite direction, they need also to be detected on opposite sides of the scanner. This has to be taken into account, while searching the coincidence events.

We start to investigate the time window of the singles from the beginning of the list. If coincidence of the event is found inside its window, a coincidence event is registered. Otherwise, the event is discarded and the next event is taken for investigation. Since a time window of 3 ns is used for this work (see Section 5.1), 1.5 ns before and after the event, must be examined. While investigating the time window of a single event, three different cases can be encountered. These are:

- One event inside the window is found, which is from a different module than the event under study. In this case a coincidence event is recorded (see Figure 5.3 (a)).
- One event inside the window is found, but it is from the same module as the initial single event. Since a photon pair cannot hit detectors of the same module (the photon pair travel in opposite direction) the resulted coincidence event is discarded (see Figure 5.3 (b)).
- More than one event is observed inside the window (multiple events). This case is illustrated in Figure 5.3 (c). Since it is not possible to decide which one of the found events is coincident of the event under study; resulting coincidence event is discarded.

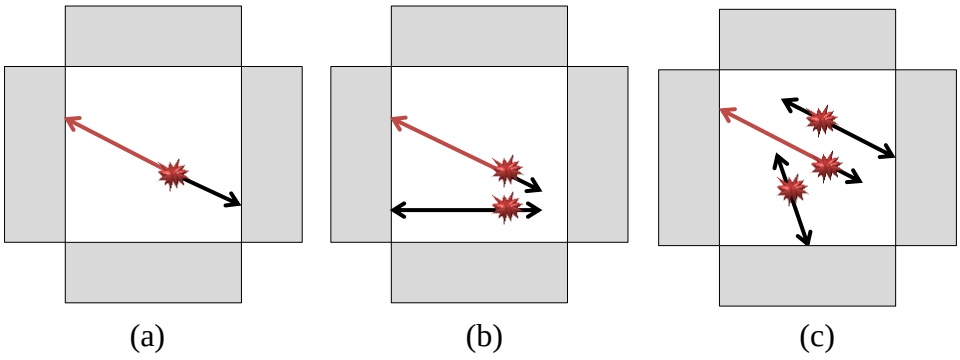

***Figure 5.3**. Illustration of different cases that may occur, while investigating the coincidence window of a single event. The red arrow indicates the event under study. (a) Only one event is found in the window (the event is from different module). (b) Only one event is found, but it is from the same module. (c) Two events are detected inside the window (multiple events).*

As discussed before, currently constructed PET camera is just a prototype and additional layers may are built up above the current modules or besides them in the future (see Figure 5.4). For such scanner an additional case has to be taken into account. As there is more than one module on each side of this scanner, the detection of the photon pair in different modules does not guarantee their detection to the opposite sides of the scanner. Thus, in order to identify whether the photon pair are detected on opposite sides, the label of the modules can be utilized. In other words, if the first parameter of the label of the detecting modules is the same, it indicates that they are on the same side of the scanner and thus the resulted coincidence event is discarded. For instance, in Figure 5.4 the event under study is shown with red and the found event is shown with black. As detecting modules have the same value i.e. *1* as the first parameter of their labels, the resulted coincidence event is not accepted.

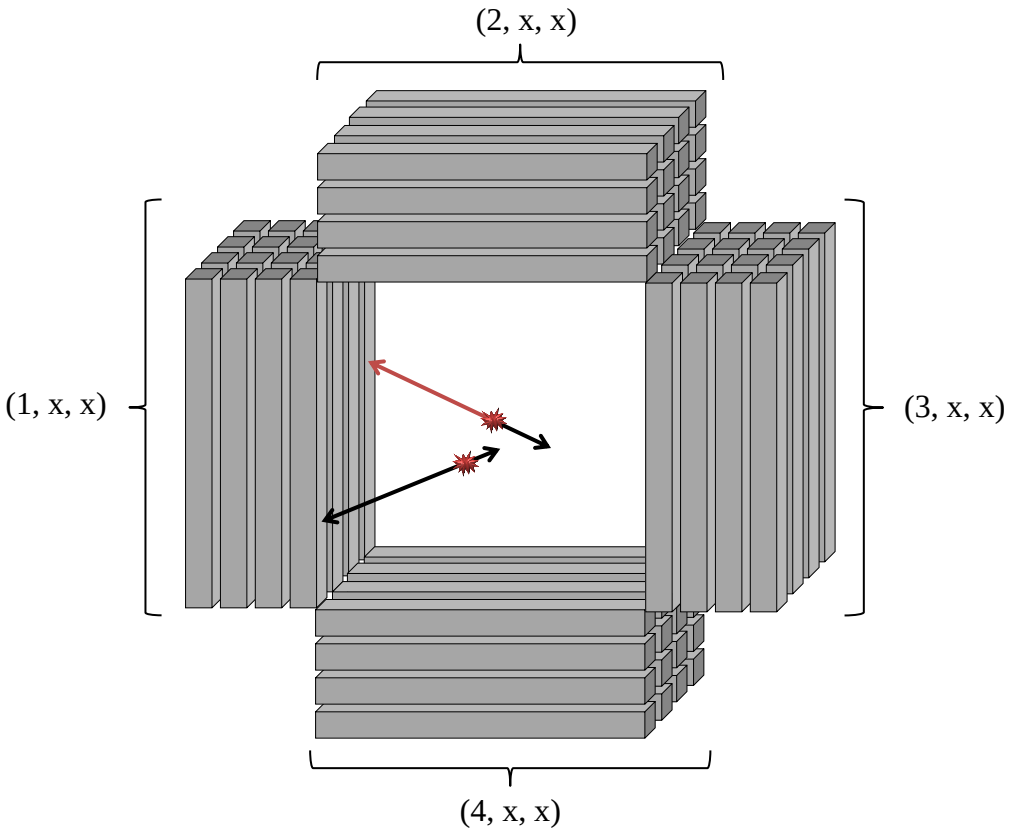

Figure 5.4. *AvanTomography demonstrator with four layers in axial direction and four layers in transaxial direction. The parameters shown with letter "x" in the module IDs get the value 1-4 based on the position of the module in the scanner.*

In this thesis, just one layer is assumed for the scanner and the codes are implemented for the scanner made of one module layer. Pseudocode *Check Coincidence Window* illustrates how coincidence window of an event is investigated. For each event as much as half the coincidence window (1.5 ns) before it and half the window after it, is examined. In order to avoid mix up between the events, we call the event for which the coincidence window is under study as *event x.* Before the execution of the code a vector is created for saving the indexes of the events found inside the window. This vector is called as *indexes.*

In the first **while** loop 1.5 ns before the *event x* is checked. At each iteration of the loop an event is selected for checking its time stamp. In first iteration (at line 4) the previous word of the *event x* is selected and (at line 5) its timestamp is compared to the timestamp of the *event x.* The **if** statement checks whether the difference time is smaller than 1.5 ns, the index of the selected event is saved in the vector *indexes* and pointer is moved to the previous event in the list. The loop is stopped, when one of the next conditions is fulfilled:

- The difference time between the selected event and *event x* is bigger than 1.5 ns.

- The pointer reaches to the beginning of the list i.e. all the events before the *event x* are considered.

The next **while** loop investigates the events, which are placed in the list after the *event x*, i.e. 1.5 ns after it, is examined. Different steps of the loop are executed in the same manner as the first while loop.

```
Check Coincidence Window (event x, single events)
1     n ← index of the event x – 1
2     set counter to 1
3     while not reached to the beginning of the file (n > 0) do
4           prev ← select the previous word
5           diff ← event x.timestamp – prev.timestamp
6           if diff <= 1.5 then
7             indexes[i] ← n
8             move to the previous word (decrement n by 1)
9             increment counter
10          else
11            end while loop
12          end if
13    end while
14
15    n ← index of the event x + 1
16    while not reached to the end of the file (n <= amount of single events) do
17          next ← select the next word
18          diff ← next.timestamp – event x.timestamp
19          if diff <= 1.5 then
20            indexes[i] ← n
21            move to the next word (increment n by 1)
22            increment counter
23          else
24            end while loop
25          end if
26    end while
```

After the execution of the above presented code, the vector *indexes* are checked. If they contain only one event from different module than the *event x*, this event called as *event y* is selected for further consideration. The same code is run also for *event y*. If similarly only one event from different module is found in the time window of the *event y*, the two events (*event x* and *event y*) are assumed as coincidences and a coincidence event is recorded. This is illustrated in the code *Find Coincidence Events*.

```
Find Coincidence Events (single events)
1     ind ← 1
2     while ind <= amount of single events do
3           event x ← event at index ind
4           indexes ← check coincidence window (event x)
5           if only one event from different module is found then
6              event y ← the found event
7              indexes2 ← check coincidence window (event y)
8              if only one event from different module is found then
9                 Register the event x and event y as a coincidence event
10                ind ← ind + 2
11             else
12                ind ← ind + 1
13             end if
14          else
15             ind ← ind + 1
16          end if
17    end while
```

5.5 Raw data construction

Once the coincidence events of a predefined time window for instance 1 s have been defined, using the methods explained in Section 5.3 the axial coordinates of these events is determined. As explained in that section, depending of the size of the biggest cluster in the WLS strips of the event, one or two WLS strips may are selected as the axial coordinate of the event.

Thereafter, we write the coincidence events into a file such that each line represents a coincidence event, which consists of two single events. As Table 5.2 shows each line of the file contains 11 different fields. The first one indicates the number of coincidence event, which starts from 1 and increases gradually. The next five fields provide the information about one of the two events in a coincidence pair, while the last five fields represent relevant information about the other one. The fields *Time1, Energy1, Module1, LYSO1,* and *WLS1* represent the time stamp, energy, module ID, LYSO ID, and WLS strip ID of the first event accordingly and the fields *Time2, Energy2, Module2, LYSO2,* and *WLS2* indicate corresponding information for the second event. The format and range of the time stamp, energy, module ID, and LYSO ID values was shown in Table 5.1. The WLS strip ID of the event indicates its axial coordinate, which may contain one or two WLS strip IDs.

Table 5.2. *Illustration of different fields represented in each line of the raw data file.*

Event number	Time1	Energy1	Module1	LYSO1	WLS1	Time2	Energy2	Module2	LYSO2	WLS2

The data saved in the raw data file is used for positioning of the coincidence events after which the positioned events are transformed to the list mode file.

5.6 Positioning of interaction point

Once the coincidence events are defined and their relevant information is stored in the raw data file, we start to calculate the 3D position of these events. In order to define the position of the hit in the scanner coordinate system, first intramodular hit location must be calculated.

5.6.1 Intramodular hit location

As discussed before, LYSO crystals are used for determination of the X and Y-coordinates of the hit and WLS strips determine the Z-coordinate of it. In Section 4.1 was explained how the intramodular coordinate system is defined. For calculating the intramodular position of the hit, first we need to determine the center point of the module in all directions.

In order to calculate the center of module in X- and Y-directions, the size of the crystals and distance between them as well as distance of the crystals to the module borders should be taken into account. Figure 5.5 (a) illustrates how crystals are set up inside a module and what are different distances between crystals and module borders. The transaxial size of the crystals is 3×3 mm^2 and there is an air gap of 0.5 mm between them in a layer. The crystals in different layers are also distanced by 0.5 mm. Other distances taken into account are d1 = 1 mm, d2 = 1.5 mm, d3 = 2.7 mm, d4 = 2.8 mm, d5 = 3 mm, d6 = 10 mm, and d7 = 15 mm (see Figure 5.5). Using these information the center of module in the mentioned directions is calculated. This point is assigned as point *O* in Figure 5.5 (a).

In the same way, using the WLS strips and distances between them, the center of module in Z-direction is determined. The WLS strips are of 3 mm width and there is a gap of 0.5 mm between them. Figure 5.5 (b) shows the midpoint of the WLS strip with label 22 assigned as the center of the module in axial direction.

Consequent to the determination of the center of the module, distance of the hit (in three directions) with respect to the module center is calculated. This provides the intramodular 3D position of the hit, which must be converted to intermodular coordinate system to obtain the actual position of the photon interaction point.

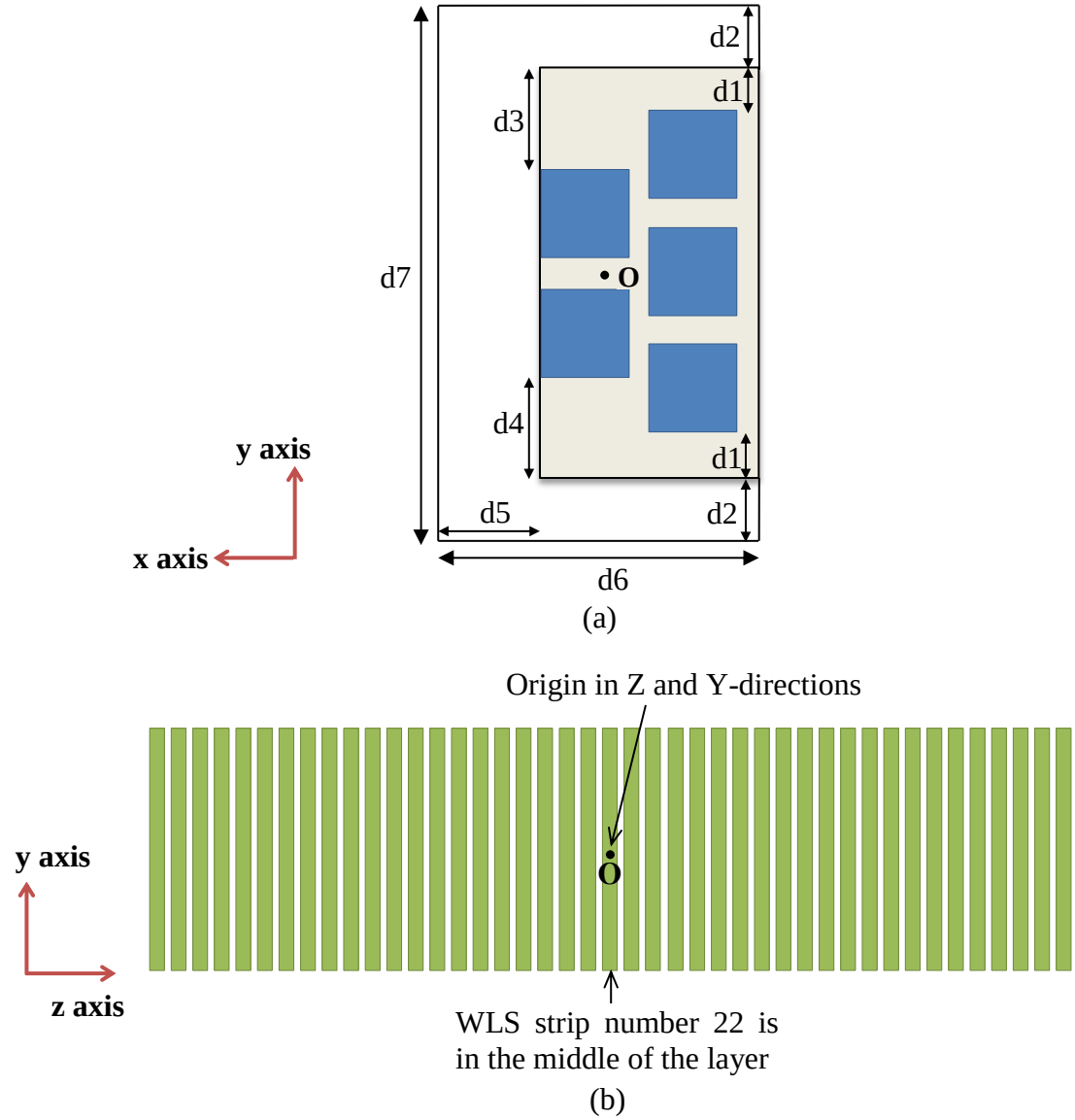

Figure 5.5. *Determination of the center of module in 3D coordinates. Calculated center of module is assigned as "O" in both figures (the center point has not been calculated to the center of the detectors, but to the center of modules). (a) Set up of the crystals inside a module. The distances d1, d2, d3, d4, d5, d6, and d7 equal to 1 mm, 1.5 mm, 2.7 mm, 2.8 mm, 3 mm, 10 mm, and 15 mm accordingly . (b) A layer of WLS strips, which is aligned in axial direction above the crystal layers.*

5.6.2 Location of modules in the scanner

In order to convert the intramodular hit location to the intermodular coordinate system; we need to first determine the position of each module in the scanner. Location of the module can be defined using its two end points. We choose the center point at each end of the module as the mentioned points. These points are assigned as *point a* and *point b* for module *(4, 1, 1)* in Figure 5.6. Point *O* indicates the center point of the module *(4, 1, 1)*.

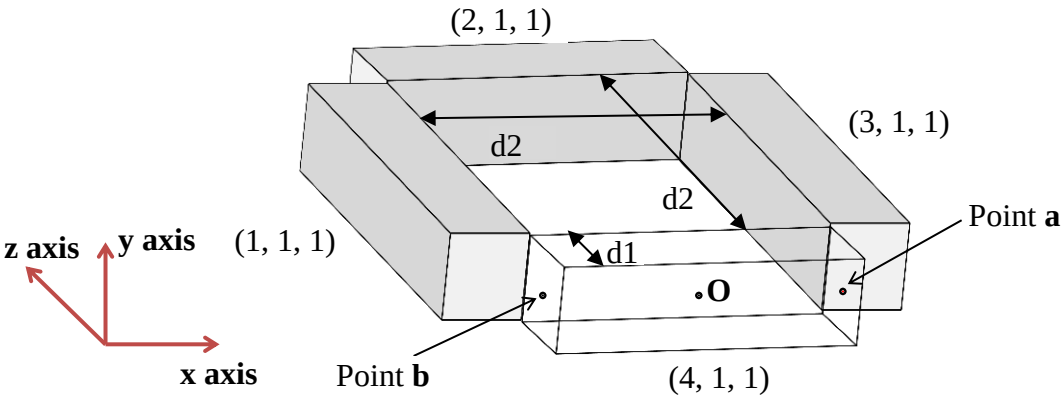

Figure 5.6. *Illustration of the two endpoints used to determine the location of the modules in the scanner. These points are assigned as "point a" and "point b" for the module (4, 1, 1). The center of the module is assigned as "O". The distances d1 and d2 equal to 10 mm and 150 mm.*

For each module the 3D coordinates of points *a* and *b* (shown in Figure 5.6) with respect to the scanner center are calculated. The distances between two opposite modules in the scanner as well as the depth of modules (d2 and d1 in Figure 5.6) are used for calculation the position of these points. Pseudocode *Get module ends* illustrates how 3D coordinates of the points *a* and *b* for each module are defined. This function gets the module label as input and defines the 3D location of the mentioned points for the input module, where X-, Y- and Z-coordinates of point *a* is assigned as x_a , y_a, and z_a and corresponding coordinates of the point *b* is assigned as x_b, y_b, and z_b.

Once positions of the points *a* and *b* are defined for the modules, 3D coordinates of the center point of the modules (point *O* in Figure 5.6) can be simply determined by dividing the coordinates of the endpoints by 2. Table 5.3 shows the defined 3D coordinates of the two endpoints of the modules as well as their center point. The columns 1-4 of the table indicate the label of the module, the 3D dimension of the point *a* in the module, the 3D dimension of the point *b*, and the location of the center of the module accordingly. Consequently, using the intermodular 3D coordinates of the module center and the defined intramodular hit location in Subsection 5.6.1, intermodular position of the hit can be determined.

Get module ends (module label)
1 **if** *module label is (1, 1, 1)* **then**
2 $x_a \leftarrow -((d2/2) + (d1/2))$
3 $y_a \leftarrow 0$
4 $z_a \leftarrow -(d2/2)$
5 $x_b \leftarrow x_a$
6 $y_b \leftarrow y_a$
7 $z_b \leftarrow -z_a$
8 **else if** *module label is (2, 1, 1)* **then**
9 $x_a \leftarrow -(d2/2)$
10 $y_a \leftarrow 0$
11 $z_a \leftarrow (d2/2) + (d1/2)$
12 $x_b \leftarrow -x_a$
13 $y_b \leftarrow y_a$
14 $z_b \leftarrow z_a$
15 **else if** *module label is (3, 1, 1)* **then**
16 $x_a \leftarrow (d2/2) + (d1/2)$
17 $y_a \leftarrow 0$
18 $z_a \leftarrow (d2/2)$
19 $x_b \leftarrow x_a$
20 $y_b \leftarrow y_a$
21 $z_b \leftarrow -z_a$
22 **else**
23 $x_a \leftarrow (d2/2)$
24 $y_a \leftarrow 0$
25 $z_a \leftarrow -((d2/2) + (d1/2))$
26 $x_b \leftarrow -x_a$
27 $y_b \leftarrow y_a$
28 $z_b \leftarrow z_a$
29 **end if**

Table 5.3. *3D position of the two endpoints of the modules as well as center point of the modules in the scanner.*

Module label	Point “a”	Point “b”	Point “O”
(1, 1, 1)	(-80, 0, -75)	(-80, 0, 75)	(-80, 0, 0)
(2, 1, 1)	(-75, 0, 80)	(75, 0, 80)	(0, 0, 80)
(3, 1, 1)	(80, 0, 75)	(80, 0, -75)	(80, 0, 0)
(4, 1, 1)	(75, 0, -80)	(-75, 0, -80)	(0, 0, -80)

5.6.3 Intermodular hit location

Intermodular position of the hit is determined taking into account the direction of intra-modular coordinate systems with respect to the intermodular coordinate system. For instance, in module *(1, 1, 1)* the X-axis is in opposite direction with respect to the X-axis of the scanner (see Figure 5.7). Thus, in order to define the actual X-coordinate of

the hit, the intramodular X-coordinate of it is subtracted from intermodular X-coordinate of the module center. However, in this module the Y and Z axes have the same directions as the Y and Z axes of the scanner. Therefore, for calculation of the Y- and Z-coordinates of the hit, the intramodular Y- and Z-coordinates of it are added to the corresponding intermodular coordinates of the module center. The same strategy is used for determination of actual coordinates of hit in other modules. This process is illustrated in pseudocode *Convert hit location to the scanner coordinate system*.

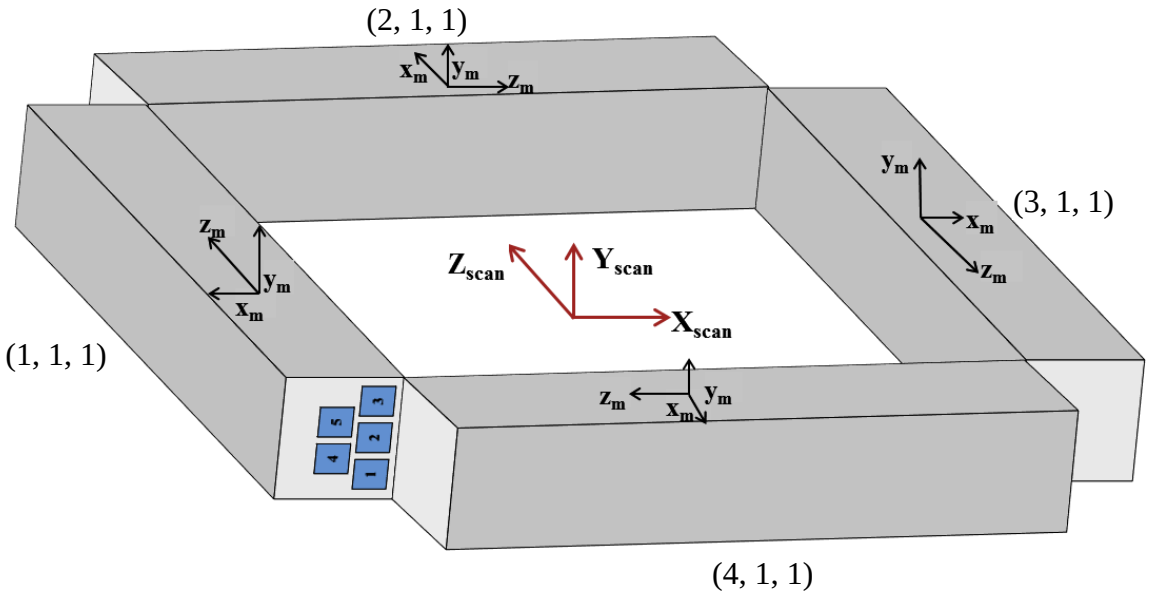

Figure 5.7. *Illustration of intramodular coordinate systems with respect to intermodular coordinate system. The intramodular 3D coordinates are shown with subscript "m" and intermodular coordinates are represented with the subscript "scan".*

The function *Convert hit location to the scanner coordinate system* gets the label of module, the intermodular coordinates of the module center point and the intramodular coordinates of the hit as input and calculates the intermodular coordinates of the hit point. In this code, *x*, *y*, and *z* indicate the intermodular position of the hit, x_{cp}, y_{cp}, and z_{cp} express the intermodular coordinates of the center point of the module, and x_{in}, y_{in}, and z_{in} represent the intramodular coordinates of the hit point.

Convert hit location to the scanner coordinate system (module label, x_{cp}, y_{cp}, z_{cp}, x_{in}, y_{in}, z_{in})

```
1    if module label is (1, 1, 1) then
2        x ← x_cp - x_in
3        y ← y_cp + y_in
4        z ← z_cp + z_in
5    else if module label is (2, 1, 1) then
6        x ← x_cp + z_in
7        y ← y_cp + y_in
8        z ← z_cp + x_in
9    else if module label is (3, 1, 1) then
10       x ← x_cp + x_in
11       y ← y_cp + y_in
12       z ← z_cp - z_in
13   else
14       x ← x_cp - z_in
15       y ← y_cp + y_in
16       z ← z_cp - x_in
17   end if
```

5.6.4 Lookup table construction

In order to expedite the positioning of the coincidence events, 3D location of all possible interaction points can be calculated beforehand and saved in the so called lookup tables. Therefore, for each detected coincidence event is not necessary to do all calculations required for defining the intramodular hit positions and then to convert those to the scanner coordinate system, but just position of the corresponding points is selected from the ready lookup tables.

Inside each module there are 85 different positions in Z-direction (43 WLS strips + midpoint between adjacent WLS strips) and two different positions in X-direction (first crystal layer and second crystal layer). These positions are illustrated in Figure 5.8 (a). As each module contains five crystals each one having different Y-coordinate, there are five different positions at this direction. Figure 5.8 (b) shows different positions at Y-direction.

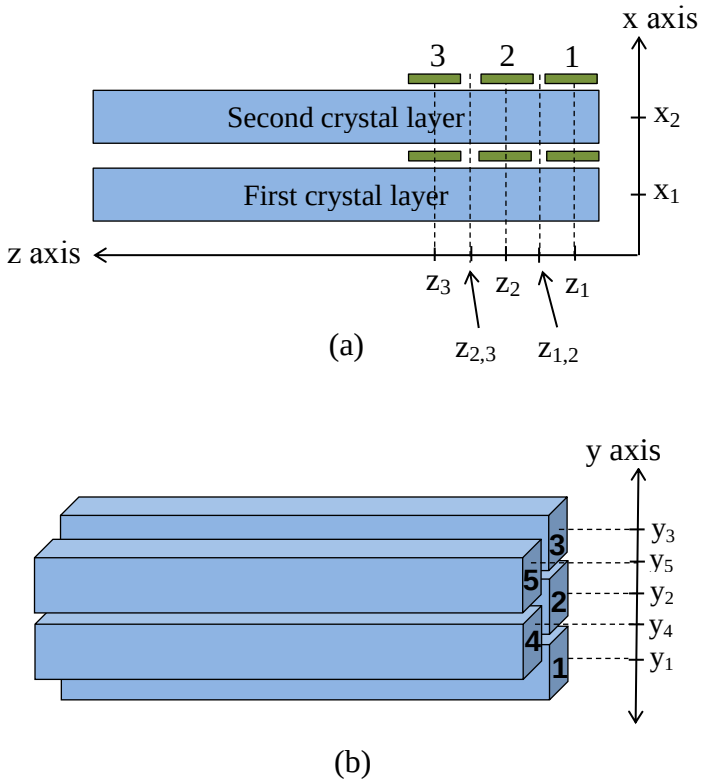

Figure 5.8. *Illustration of different 3D positions inside the modules. (a) Inside each module, the first and the second crystal layers correspond to different positions at X-direction. These positions are assigned as x_1 and x_2 for the first and the second layer. At Z-direction, the WLS strips as well as center point between each WLS strip pair correspond to different positions. In this figure, just the WLS strips (shown in green) with labels 1, 2, and 3 and their corresponding positions are illustrated. (b) Each crystal inside a module corresponds to different position in y-direction. The crystals with labels 1, 2 and 3 are located in the first layer and their Y-coordinate is indicated with y_1, y_2, and y_3. The crystals with labels 4 and 5 are located in the second layer and their Y-coordinate is assigned as y_4 and y_5.*

As was shown in pseudocode *Convert hit location to the scanner coordinate system*, the actual Z-coordinate of the hit in modules *(1, 1, 1)* and *(3, 1, 1)* is defined using the intramodular Z-coordinate of the hit ($z = z_{cp} + z_{in}$), while in modules *(2, 1, 1)* and *(4, 1, 1)*, it is defined using the intramodular X-coordinate of the interaction point ($z = z_{cp} + x_{in}$). Thus, the maximum amount of possible points in Z-direction of the scanner is 85. On the other hand, the actual X-coordinate of the hit in the modules *(2, 1, 1)* and *(4, 1, 1)* is defined by the intramodular X-coordinate of the hit ($x = x_{cp} + x_{in}$) and in the modules *(1, 1, 1)* and *(3, 1, 1)*, it is determined by the intramodular Z-coordinate of the hit ($x = x_{cp} + z_{in}$). Therefore, there are also 85 different positions in X-direction of the scanner.

As amount of the possible positions in X- and Z-direction of the scanner is the same, we create a joint lookup table for these directions. Table 5.4 shows format of the created lookup table for saving the X- and Z-coordinates of the possible points. Different rows

of the table are used for different positions in Z-direction inside the modules. I.e. the first row shows the points with the WLS strip number *1* as their Z-coordinate and the second row shows the points, which have the midpoint between the WLS strip number *1* and number *2* as their Z-coordinate and so on. The first two columns of the table show the positions, which belong to the first crystal layer and as it is marked in the table, in the first column the X-coordinate of the points is saved, while in the next column Z-coordinate of the mentioned points is recorded. The third and fourth columns show the points at the second crystal layer. Since possible points in different modules have different X- and Z-coordinates with respect to the scanner center, separate tables are created for different modules resulting in four tables for the mentioned two directions. In addition for each added module to the scanner, one similar lookup table must be created for the X- and Z-coordinates of the possible interaction points.

Table 5.4. *Illustration of the format of the table used for saving the X- and Z-coordinate of the possible interaction points. The locations assigned as p in the table, will be replaced by the calculated coordinates of the points.*

	First crystal layer		**Second crystal layer**	
WLS ID	$\mathbf{X_{scan}}$	$\mathbf{Z_{scan}}$	$\mathbf{X_{scan}}$	$\mathbf{Z_{scan}}$
1	p	p	p	p
1, 2	p	p	p	p
2	p	p	p	p
2, 3	p	p	p	p
3	p	p	p	p
⋮	⋮	⋮	⋮	⋮
43	p	p	p	p

The intermodular Y-coordinate of the interaction point is defined using the intramodular Y-coordinate of the hit in all modules i.e. $y = y_{cp} + y_{in}$. As was shown in Table 5.3, value of the y_{cp} (Y-coordinate of the center of module) is zero for all modules. Thus, the intermodular Y-coordinate of the hit is the same as intramodular Y-coordinate of that point. There are five different positions at Y-direction inside each module and all the existent modules contain the same possible positions in Y-direction with respect to the scanner center. Therefore, one table is created for saving Y-coordinate of the points and is used jointly for all existing modules. However, if additional modules are constructed above the current ones (at Y-direction), for each added module layer, separate lookup table must be created for Y-direction. The reason is that the new module layers have different Y-coordinates than the current one, thus they have different possible interaction points at this direction.

Table 5.5. *Illustration of the format of the created table for recording Y-coordinate of the possible points of all existing modules.*

LYSO ID	Y_{scan}
1	p
2	p
3	p
4	p
5	p

5.6.5 Interaction point determination from lookup tables

When 3D coordinates of all possible positions are calculated and recorded in lookup tables, we can determine the actual positions of the coincidence events just by selecting X- , Y- and Z-coordinates of the corresponding points from the ready lookup tables.

Next pseudocodes illustrate how the coincidence events are positioned from the lookup tables, which are constructed beforehand. As mentioned in Subsection 5.6.4, four tables are created for the X- and Z-coordinates of the hit points, one table for each module. These tables are called as *table_1*, *table_2*, *table_3* and *table_4* for modules *(1, 1, 1)*, *(2, 1, 1)*, *(3, 1, 1)*, and *(4, 1, 1)* accordingly. The format of the mentioned tables is as Table 5.4. For Y-coordinate of the hit points one table is used jointly for all modules (see Table 5.5). This table is called as *table_y*.

The pseudocode *Define Actual Position of a Coincidence Event* searches for the coordinates of an event pair from the constructed tables. As each coincidence event contains two events, the for loop cycles two times, once for each event. At line 2, an event is selected from the event pair. At lines 3-5, the module, LYSO ID and WLS strip of the event are saved in parameters *mod*, *lyso*, and *wls* accordingly. At line 7, Y-coordinate of the event is selected from the table *table_y*. At line 8, in order to define the row and columns of the table, at which the X- and Z-coordinate of the event are recorded, the function *Decide Index* is called. The pseudocode of this function is also presented. Once the row and columns of the table for the X- and Z-coordinate of the event are defined, at lines 9-11 the function checks whether the module label is *(1, 1, 1)*, the mentioned coordinates of the event are selected from the table *table_1*. Similarly, in next branches of the **if** statement the actual coordinates are selected from the corresponding tables.

The function *Decide Index* gets LYSO ID and WLS strip of the event as input. At lines 1-3 of this function, if LYSO ID is *1*, *2* or *3*, first column of the table is selected for the X-coordinate of the event and second column of the table is selected for the Z-coordinate of it. At lines 4-6, if LYSO ID is *4* or *5*, third column of the table is selected for the X-coordinate of the event and fourth column is selected for the Z-coordinate of the event. At lines 8-12, the function checks whether only one WLS strip is saved as the *wls* of the event (the case of odd size for the biggest cluster of the event, explained in

Section 5.3) or two WLS strips are recorded as its *wls* (even cluster size). The corresponding row of the table for both cases is calculated.

```
Define Actual Position of a Coincidence Event (coincidence event)
1     for ind ← 1 to 2
2         event ← event at index ind
3         mod ← module label of the event
4         lyso ← lyso ID of the hit
5         wls ← WLS strip of the hit
6
7         y ← select from table_y the value at row "lyso"
8         [r, colx, colz] ← Decide Index (lyso, wls)
9         if mod is (1, 1, 1) then
10            x ← select from table_1 the value at row "r" and column "colx"
11            z ← select from table_1 the value at row "r" and column "colz"
12        else if mod is (2, 1, 1) then
13            x ← select from table_2 the value at row "r" and column "colx"
14            z ← select from table_2 the value at row "r" and column "colz"
15        else if mod is (3, 1, 1) then
16            x ← select from table_3 the value at row "r" and column "colx"
17            z ← select from table_3 the value at row "r" and column "colz"
18        else
19            x ← select from table_4 the value at row "r" and column "colx"
20            z ← select from table_4 the value at row "r" and column "colz"
21        end if
22    end for
```

```
Decide Index (lyso, wls)
1     if lyso is "1" or "2" or "3" then
2         colx ← first column of the table
3         colz ← second column of the table
4     else
5         colx ← third column of the table
6         colz ← last column of the table
7     end if
8     if wls contains one WLS strip
9         r ← (wls × 2) - 1
10    else
11        r ← (first WLS strip label + second WLS strip label) – 1
12    end if
```

6 RESULTS

In this chapter result of the implemented methods are represented. As a real data was not available for this work, in order to test the built programs, a simulated test data was created manually. This data was used for the evaluation of the approaches used for coincidence detection and determination of the 3D position of the coincidence events.

6.1 Test data construction

Since generating test data manually is not easy and it needs Monte Carlo simulations, we built a data containing 20 event words for testing the methods. These events have energy values between 400-600 keV. Thus, it was assumed that only events in coincidence were present. Table 6.1 illustrates the generated data.

Each row of the Table 6.1 represents an event word, where each word contains 5 fields expressed in columns of the table. The columns 1-5 show the time stamp, energy, module of interaction, LYSO crystal of interaction and a layer of WLS strips for the corresponding event. The last column of the table shows the WLS strips data of the corresponding event. In order to exhibit 43 WLS strips with values “0” or “1”, only indexes of the WLS strips with value “1” are represented. This means that the rest of WLS strips have the value “0”. The indexing of the WLS strips starts from 1 and continues to 43. For instance, the WLS strip data of the event expressed at the first row specifies that the WLS strips with IDs *5-7*, *10-16*, and *18-20* have value “1” and the rest WLS strips have the value “0”.

Table 6.1. *Single events with energy in 400-600 keV. These events are used for evaluation of the implemented methods.*

	Time stamp	Energy	Module	LYSO	WLS strip
1	1	454	(1, 1, 1)	2	(5-7, 10-16, 18-20) = 1
2	2	400	(3, 1, 1)	3	(1-3, 20-26) = 1
3	5	410	(1, 1, 1)	3	(10-13, 20-26) = 1
4	6	502	(2, 1, 1)	3	(10-13, 20-26, 27-30) = 1
5	7	500	(3, 1, 1)	2	(10-13, 20-26) = 1
6	9	477	(4, 1, 1)	4	(27-30) = 1
7	10	545	(2, 1, 1)	2	(10-13, 20-26) = 1
8	12	540	(1, 1, 1)	1	(10-13, 20-26) = 1
9	14	530	(3, 1, 1)	5	(1-2) = 1
10	15	402	(1, 1, 1)	4	(1-7, 27, 37-38) = 1
11	17	561	(1, 1, 1)	1	(20-25, 27) = 1
12	18	516	(2, 1, 1)	4	(10, 12, 37-38) = 1
13	20	582	(1, 1, 1)	3	(42-43) = 1
14	21	533	(1, 1, 1)	4	(30-32) = 1
15	23	407	(3, 1, 1)	4	(15-18) = 1
16	24	407	(2, 1, 1)	3	(15-22) = 1
17	26	533	(4, 1, 1)	1	(30-32) = 1
18	28	516	(1, 1, 1)	2	(10, 12, 37-38) = 1
19	29	516	(2, 1, 1)	4	(10, 12-13, 37-38) = 1
20	31	502	(4, 1, 1)	3	(10-13, 20-26, 27-30) = 1

6.2 Raw data file

The data represented in Table 6.1 is selected for coincidence detection. The coincidence events are defined using a program, which is illustrated in the pseudocode *Find Coincidence Events* presented in Section 5.4. Consequently, axial coordinate of the coincidence events is defined using the approaches described in Section 5.3. Next, the coincidence events with the determined axial coordinate are recorded into a raw data file. The content of this file is shown in Table 6.2.

Each row of the file represents a coincidence event and the relevant information of the event is expressed at its columns. The first column of the file shows the coincidence event number and as shown in the figure, five coincident events are found from the given data. As mentioned in previous section, our data consists of 20 single events, though only 10 events among them are included in coincidence events and the rest are discarded. The reasons for discarding these events were explained in Section 5.4. The columns titled with *Time1*, *Eng1*, *Mod1*, *LYSO1* and *WLS1* represent time of occurrence, energy,

the module of interaction, the LYSO and the WLS strip of the hit for one of the event pair, accordingly. The columns *Time2*, *Eng2*, *Mod2*, *LYSO2* and *WLS2* represent similar information for the other event of the coincidence pair.

Table 6.2. *Content of the raw data file.*

Event	Time1	Eng1	Mod1	LYSO1	WLS1	Time2	Eng2	Mod2	LYSO2	WLS2
1	1	454	1	2	13	2	400	3	3	23
2	9	477	4	4	28,29	10	545	2	2	23
3	14	530	3	5	1,2	15	402	1	4	4
4	17	561	1	1	22,23	18	516	2	4	37,38
5	23	407	3	4	16,17	24	407	2	3	18,19

6.3 Lookup tables

The 3D coordinate of all possible points inside the modules are calculated beforehand and recorded in the lookup tables. Four lookup tables are created for saving X- and Z-coordinates of the points, one table for each module. For recording Y-coordinate, one table is created, which is used jointly for all the existing modules.

The lookup tables used for X- and Z-coordinates contain 85 rows, where each row represents the corresponding coordinates for every position in axial direction inside the modules. Table 6.3 indicates the first 19 rows of such table created for module *(1, 1, 1)*. First column of the table represents the ID of the WLS strip, for which the mentioned coordinates are calculated. Thus, in rows with one WLS strip the corresponding coordinates for the center point of the relative WLS strip are recorded, while in rows with two WLS strips (separated by comma), the corresponding coordinates for the center point between the mentioned two WLS strips are saved. Second and third columns of the table show the X- and Z-coordinates of the points in the first crystal layer and the last two columns indicate the corresponding coordinates of the points in the second crystal layer of the module. The complete tables of the mentioned coordinates for all possible positions inside the modules are represented in Appendix 1.

The lookup table created for recording the Y-coordinate of the possible points in the modules contains five rows, where each row indicates the Y-coordinate of each LYSO crystal in the modules. Table 6.4 represents this lookup table, which is used jointly for all modules.

Table 6.3. *The first 19 rows of the created lookup table for recording the X- and Z-coordinates of the points in module (1, 1, 1).*

	First crystal layer		Second crystal layer	
WLS ID	**X_{scan}**	**Z_{scan}**	**X_{scan}**	**Z_{scan}**
1	-77	-73.5	-80.5	-73.5
1, 2	-77	-71.75	-80.5	-71.75
2	-77	-70	-80.5	-70
2, 3	-77	-68.25	-80.5	-68.25
3	-77	-66.5	-80.5	-66.5
3, 4	-77	-64.75	-80.5	-64.75
4	-77	-63	-80.5	-63
4, 5	-77	-61.25	-80.5	-61.25
5	-77	-59.5	-80.5	-59.5
5, 6	-77	-57.75	-80.5	-57.75
6	-77	-56	-80.5	-56
6, 7	-77	-54.25	-80.5	-54.25
7	-77	-52.5	-80.5	-52.5
7, 8	-77	-50.75	-80.5	-50.75
8	-77	-49	-80.5	-49
8, 9	-77	-47.25	-80.5	-47.25
9	-77	-45.5	-80.5	-45.5
9, 10	-77	-43.75	-80.5	-43.75
10	-77	-42	-80.5	-42

Table 6.4. *Lookup table representing the Y-coordinate of the possible points in all modules.*

LYSO ID	Y_{scan}
1	-3,5
2	0
3	3,5
4	-1,7
5	1,8

6.4 3D position of the coincidence events

Consequent to determination of the 3D coordinates of all possible positions of the modules and recording them into lookup tables, the corresponding coordinates of the coincidence events are selected from these tables. The way how to define the rows and col-

umns of the corresponding coordinates of the event in the lookup tables, was described in Subsection 5.6.5. Therefore, 3D positions of the coincidence events presented in Table 6.2 are determined and then saved in a list mode file format. Table 6.5 shows the content of the resulted file.

Each row of Table 6.5 represents the location of the events from one coincidence event such that a single row shows the location of the events represented in corresponding row of Table 6.2. The columns 1-3 show the 3D coordinates of one event of the coincidence pair and the columns 4-6 represent the corresponding coordinates of the other event of the event pair.

Table 6.5. *Illustration of the 3D position of the obtained coincidence events.*

X1	Y1	Z1	X2	Y2	Z2
-77	0	-31.5	77	3.5	-3.5
-22.750	-1.7	-80.5	3.5	0	77
80.50	1.8	71.75	-80.5	-1.7	-63
-77	-3.5	1.75	54.25	-1.7	80.5
80.5	-1.7	19.25	-12.25	3.5	77

7 DISCUSSION AND CONCLUSION

This thesis provides the methods for coincidence detection and positioning of the coincidence events in AvanTomography demonstrator. Positions of the coincidence events were defined using the intramodular hit position and then these positions were converted to the intermodular coordinate system. Furthermore, lookup tables were created for fast positioning of the coincidence events, in which 3D location of all possible interaction points were recorded.

Scintillating LYSO crystals and WLS strips constitute the main components of the AvanTomography demonstrator providing 3D coordinates of the coincidence events. The crystals and WLS strips are read individually using the connected APD detectors leading to 364 different channels in the system. In order to be able to identify module of interaction, crystal of interaction and corresponding WLS strip/strips, individual labels for each one of these components were determined.

For testing our methods, we created 20 event words with MATLAB. Each event word holds information on the time of detection, energy of the event as well as the module and the LYSO crystal of interaction and a layer of WLS strips. The data of the WLS strips is used for defining Z-coordinate of the interaction point. For this purpose we employed a *clustering* algorithm on the data of the layer of WLS strips to find the biggest cluster of the WLS strips above the threshold and then we applied the *center of gravity* method on the found cluster. As the result, one or two WLS strips were selected for defining the Z-coordinate of the event. The single event words were used for defining the coincidence events. The resulting coincidence events are shown in Table 6.2.

For determination of the position of the interaction point, first we defined the intramodular 3D coordinates of the hit taking into account the size of the crystals and the distances between them (hit location in transaxial direction) as well as the width of the WLS strips (hit location in axial direction). Consequently, the defined location was converted into intermodular coordinate system. In order to speed up the determination of location of the coincidence events, we utilized lookup tables such that 3D position of every possible interaction point in the scanner was calculated beforehand and recorded in these tables. Therefore, it was not necessary to repeat the calculation of the position of each detected event. Instead, based on the hit module, crystal and the decided WLS strip/strips as Z-coordinate of the event, the position of the event was selected from the lookup tables. We created separate tables for saving the X- and Z-coordinates of the interaction points in each module resulting in four tables for the mentioned directions. These tables are illustrated in Appendix 1. For recording Y-coordinate of the hit points, a joint table shown in Table 6.4 was created and used for all existing modules. Subse-

quently, position of the coincidence events was defined using the constructed lookup tables and recorded in a list mode file format. The content of this file is represented in Table 6.5. The time used for defining the position of coincidence events was calculated 0.020236 seconds with a PC.

Utilization of the lookup tables was verified as an efficient and fast way for positioning the coincidence events. Although our test data was small, this approach can be very useful in real PET applications, where large amount of coincidence events are detected. Moreover, the given methods can be used in construction of lookup tables for additional module layers in the scanner, in the future.

Adding layers at different directions of the scanner leads to construction of different amount of lookup tables for the new modules. Here, in order to be easier to refer to different types of lookup tables, we call the lookup table, where X- and Z-coordinates of the events are recorded as XZ-lookup table and the table, where Y-coordinate of the events is recorded as Y-lookup table. If additional module layers are constructed in Y-direction of the scanner (larger FOV, see Figure 7.1), as only Y-coordinate of the new modules is changed with respect to the modules on the first layer; for every new layer just a Y-lookup table is required. For the X- and Z-coordinates of the events the corresponding tables, which were created before for the modules of the first layer, can be used. For instance, all the modules with label (1, 1, x), where x has a value from 1-4, can use the same XZ-lookup table (but different Y-lookup tables). The same statement is also valid for the modules (2, 1, x), (3, 1, x) and (4, 1, x). Since each XZ-lookup table occupies 2720 bytes, using the existing XZ-lookup tables for the new layers saves memory space. As a Y-lookup table occupies 40 bytes, each added layer in Y-direction requires additional 40 bytes.

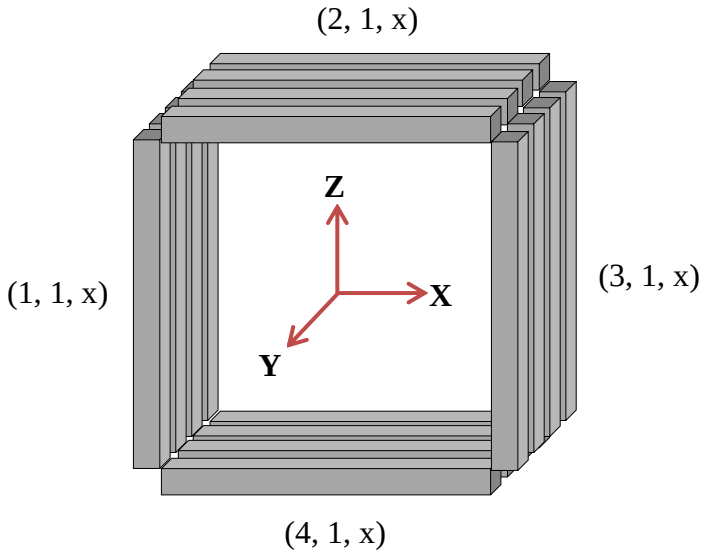

Figure 7.1. *Additional module layers in Y-direction of the scanner. The label of the modules at each side of the scanner is shown. The letter x in the labels can get the values 1-4 for modules with different Y-coordinates.*

However, if additional layers are constructed in X- and Z-direction of the scanner (see Figure 7.2), the number of created lookup tables is different than adding them in Y-direction. In this case, the added modules have the same Y-coordinate as the modules on the first layer. Thus, the Y-lookup table of the first layer can be used for the new layers. However, XZ-lookup tables must be created separately for the new modules. Thus, each additional layer in X- and Z-direction of the scanner results in $4 \times 2720\text{bytes} = 10880\text{bytes}$ of memory.

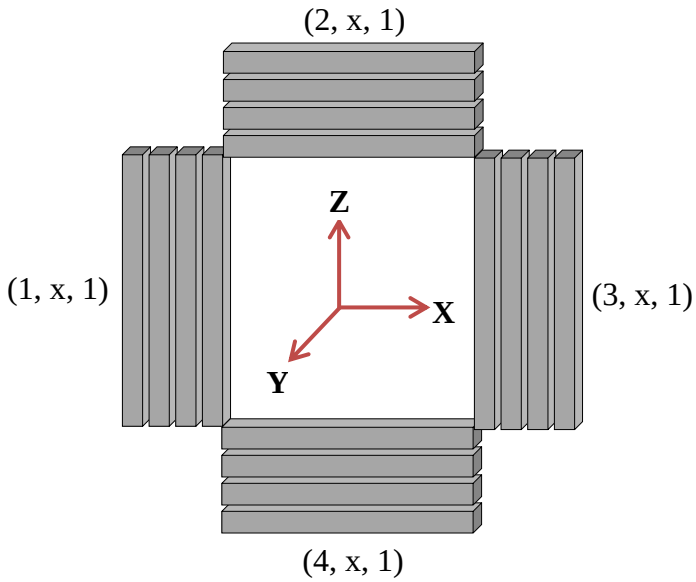

Figure 7.2. *Additional module layers in X- and Z-direction of the scanner. The label of the modules at each side of the scanner is shown. The letter x in the labels can get the values 1-4 for modules with different X- or Z-coordinates.*

Therefore, adding module layers for both cases explained above increase required memory for the lookup tables linearly. Moreover, additional module layers in both cases result in additional detected events as well, which leads more memory required for saving the increased amount of event words. Thus, when more layers are constructed in the scanner, certain amount of bits can be distributed among several processors.

REFERENCES

[1] *A history of medical imaging*. Retrieved November 27, 2013, from http://www.infinityugent.be/research-development/a-history-of-medical-imaging

[2] Vieira da Silva, S. M. (2011). *Study of Compton scattering in PET* (M.Sc. thesis). Department of Physics, University of Coimbra, Faculty of science and Technology, Coimbra, Portugal.

[3] Saha, G. B. (2010). *Basics of PET imaging: physics, chemistry, and regulations.* Springer.

[4] Kitson, S. L., Cuccurullo, V., Ciarmiello, A., Salvo, D., & Mansi, L. (2009). *Clinical Applications of Positron Emission Tomography (PET) Imaging in Medicine: Oncology, Brain Diseases and Cardiology.* Curr Radiopharm, 2, 224-53.

[5] Beltrame, P., Bolle, E., Braem, A., Casella, C., Chesi, E., Clinthorne, N., ... & Weilhammer, P. (2009, October). *First results from the AX-PET demonstrator*. In Nuclear Science Symposium Conference Record (NSS/MIC), 2009 IEEE (pp. 3096-3101). IEEE.

[6] Beltrame, P., Bolle, E., Braem, A., Casella, C., Chesi, E., Clinthorne, N., ... & Weilhammer, P. (2011). *The AX-PET demonstrator—Design, construction and characterization*. Nuclear Instruments and Methods in Physics Research Section A: Accelerators, Spectrometers, Detectors and Associated Equipment, 654(1), 546-559.

[7] Tuna, U. (2008). *Cosine domain gap-filling for the PET sinograms* (M.Sc. thesis). Department of Signal Processing, Tampere University of Technology, Tampere.

[8] Ollinger, J. M., & Fessler, J. A. (1997). *Positron-emission tomography*. Signal Processing Magazine, IEEE, 14(1), 43-55.

[9] Bailey, D. L., Townsend, D. W., Valk, P. E., & Maisey, M. N. (Eds.). (2005). *Positron emission tomography: basic sciences*. Springer.

[10] Clinical Jadvar, H., & Parker, J. A. (2005). *Clinical PET and PET/CT*. Springer Verlag.

[11] Steinman, A. H. (1997). *A simulator for small positron emission tomography cameras* (Doctoral dissertation, University of Toronto).

[12] Badawi, R. (1999, Jan 12). *Introduction to PET physics*. Retrieved November 9, 2013, from http://depts.washington.edu/nucmed/IRL/pet_intro/intro_src/section2.html

[13] Cherry, S. R., & Dahlbom, M. (2006, January). *PET: physics, instrumentation, and scanners*. In PET (pp. 1-117). Springer New York.

[14] Chandra, R. (2011). *Nuclear Medicine Physics: the Basics*. Lippincott Williams & Wilkins.

[15] Braem, A., Chamizo, M., Chesi, E., Colonna, N., Cusanno, F., De Leo, R., ... & Zaidi, H. (2004). *Novel design of a parallax free Compton enhanced PET scanner*. Nuclear Instruments and Methods in Physics Research Section A: Accelerators, Spectrometers, Detectors and Associated Equipment, 525(1), 268-274.

[16] Nichols, T. E., Qi, J., Asma, E., & Leahy, R. M. (2002). *Spatiotemporal reconstruction of list-mode PET data*. Medical Imaging, IEEE Transactions on, 21(4), 396-404.

[17] Watabe, H., Matsumoto, K., Senda, M., & Iida, H. (2006). *Performance of list mode data acquisition with ECAT EXACT HR and ECAT EXACT HR+ positron emission scanners*. Annals of nuclear medicine, 20(3), 189-194.

[18] Cherry, S. R., Sorenson, J. A., & Phelps, M. E. (2012). *Physics in nuclear medicine*. Elsevier Health Sciences.

[19] Shimizu, K., Ohmura, T., Watanabe, M., Uchida, H., & Yamashita, T. (1988). *Development of 3-D detector system for positron CT*. Nuclear Science, IEEE Transactions on, 35(1), 717-720.

[20] *BGO, LYSO and GSO Crystal Scintillators*. Retrieved November 24, 2013, from http://www.omegapiezo.com/crystal_scintillators.html

[21] Casella, C. (2012, March 14). *Demonstration of a novel PET concept*. Retrieved November 10, 2013, from http://dpnc.unige.ch/seminaire/talks/casella.pdf

[22] Beltrame, P., Bolle, E., Braem, A., Casella, C., Chesi, E., Clinthorne, N., ... & Weilhammer, P. (2011, October). *The AX-PET concept: New developments and tomographic imaging.* In Nuclear Science Symposium and Medical Imaging Conference (NSS/MIC), 2011 IEEE (pp. 4411-4419). IEEE.

[23] Heller, M. (2011, Jully). *AX-PET : A novel PET concept with G-APD readout,* Retrieved December 20, 2013, from, http://ndip.in2p3.fr/ndip11/AGENDA/AGENDA-by-DAY/Presentations/3Wednesday/AM/ID120-HELLER.pdf

[24] Beltrame, P., Bolle, E., Braem, A., Casella, C., Chesi, E., Clinthorne, N., ... & Weilhammer, P. (2010, October). *AX-PET: Concept, proof of principle and first results with phantoms.* In Nuclear Science Symposium Conference Record (NSS/MIC), 2010 IEEE (pp. 2754-2757). IEEE.

[25] Gillam, J. E., Solevi, P., Oliver, J. F., & Rafecas, M. (2012, May). *Inclusion of Inter Crystal Scatter data in PET*. In Biomedical Imaging (ISBI), 2012 9th IEEE International Symposium on (pp. 62-65). IEEE.

[26] Bolle, E., Casella, C., Chesi, E., De Leo, R., Dissertori, G., Fanti, V., ... & Weilhammer, P. (2012). *The AX-PET experiment: A demonstrator for an axial Positron Emission Tomograph*. Nuclear Instruments and Methods in Physics Research Section A: Accelerators, Spectrometers, Detectors and Associated Equipment.

[27] Beltrame, P., Bolle, E., Braem, A., Casella, C., Chesi, E., Clinthorne, N., ... & Weilhammer, P. (2011). *Demonstration of an Axial PET concept for brain and small animal imaging*. Nuclear Instruments and Methods in Physics Research Section A: Accelerators, Spectrometers, Detectors and Associated Equipment, 628(1), 426-429. (can be deleted)

[28] Zedda, T. (2013). *Construction and testing of a positron emission tomography demonstrator* (M.Sc. thesis). Department of signal Processing, Tampere University of Technology, Tampere.

APPENDIX 1: LOOKUP TABLES

Created lookup table for the X- and Z-coordinates of the possible positions in module (1, 1, 1).

	First crystal layer		Second crystal layer	
WLS ID	**X_{scan}**	**Z_{scan}**	**X_{scan}**	**Z_{scan}**
1	-77	-73.5	-80.5	-73.5
1, 2	-77	-71.75	-80.5	-71.75
2	-77	-70	-80.5	-70
2, 3	-77	-68.25	-80.5	-68.25
3	-77	-66.5	-80,5	-66.5
3, 4	-77	-64.75	-80.5	-64.75
4	-77	-63	-80.5	-63
4, 5	-77	-61.25	-80.5	-61.25
5	-77	-59.5	-80.5	-59.5
5, 6	-77	-57.75	-80.5	-57.75
6	-77	-56	-80.5	-56
6, 7	-77	-54.25	-80.5	-54.25
7	-77	-52.5	-80.5	-52.5
7, 8	-77	-50.75	-80.5	-50.75
8	-77	-49	-80.5	-49
8, 9	-77	-47.25	-80.5	-47.25
9	-77	-45.5	-80.5	-45.5
9, 10	-77	-43.75	-80.5	-43.75
10	-77	-42	-80.5	-42
10, 11	-77	-40.25	-80.5	-40.25
11	-77	-38.5	-80.5	-38.5
11, 12	-77	-36.75	-80.5	-36.75
12	-77	-35	-80.5	-35
12, 13	-77	-33.25	-80.5	-33.25
13	-77	-31.5	-80.5	-31.5
13, 14	-77	-29.75	-80.5	-29.75
14	-77	-28	-80.5	-28
14, 15	-77	-26.25	-80.5	-26.25
15	-77	-24.5	-80.5	-24.5
15, 16	-77	-22.75	-80.5	-22.75

16	-77	-21	-80.5	-21
16, 17	-77	-19.25	-80.5	-19.25
17	-77	-17.5	-80.5	-17.5
17, 18	-77	-15.75	-80.5	-15.75
18	-77	-14	-80.5	-14
18, 19	-77	-12.25	-80.5	-12.25
19	-77	-10.5	-80.5	-10.5
19, 20	-77	-8.75	-80.5	-8.75
20	-77	-7	-80.5	-7
20, 21	-77	-5.25	-80.5	-5.25
21	-77	-3.5	-80.5	-3.5
21, 22	-77	-1.75	-80.5	-1.75
22	-77	0	-80.5	0
22, 23	-77	1.75	-80.5	1.75
23	-77	3.5	-80.5	3.5
23, 24	-77	5.25	-80.5	5.25
24	-77	7	-80.5	7
24, 25	-77	8.75	-80.5	8.75
25	-77	10.5	-80.5	10.5
25, 26	-77	12.25	-80.5	12.25
26	-77	14	-80.5	14
26, 27	-77	15.75	-80.5	15.75
27	-77	17.5	-80.5	17.5
27, 28	-77	19.25	-80.5	19.25
28	-77	21	-80.5	21
28, 29	-77	22.75	-80.5	22.75
29	-77	24.5	-80.5	24.5
29, 30	-77	26.25	-80.5	26.25
30	-77	28	-80.5	28
30, 31	-77	29.75	-80.5	29.75
31	-77	31.5	-80.5	31.5
31, 32	-77	33.25	-80.5	33.25
32	-77	35	-80.5	35
32, 33	-77	36.75	-80.5	36.75
33	-77	38.5	-80.5	38.5
33, 34	-77	40.25	-80.5	40.25
34	-77	42	-80.5	42
34, 35	-77	43.75	-80.5	43.75
35	-77	45.5	-80.5	45.5
35, 36	-77	47.25	-80.5	47.25

36	-77	49	-80.5	49
36, 37	-77	50.75	-80.5	50.75
37	-77	52.5	-80.5	52.5
37, 38	-77	54.25	-80.5	54.25
38	-77	56	-80.5	56
38, 39	-77	57.75	-80.5	57.75
39	-77	59.5	-80.5	59.5
39, 40	-77	61.25	-80.5	61.25
40	-77	63	-80.5	63
40, 41	-77	64.75	-80.5	64.75
41	-77	66.5	-80.5	66.5
41, 42	-77	68.25	-80.5	68.25
42	-77	70	-80.5	70
42, 43	-77	71.75	-80.5	71.75
43	-77	73.5	-80.5	73.5

The lookup table used for saving the X- and Z-coordinates of the possible points in module (2, 1, 1).

	First crystal layer		**Second crystal layer**	
WLS ID	**X_{scan}**	**Z_{scan}**	**X_{scan}**	**Z_{scan}**
1	-73.5	77	-73.5	80.5
1, 2	-71.75	77	-71.75	80.5
2	-70	77	-70	80.5
2, 3	-68.25	77	-68.25	80.5
3	-66.5	77	-66.5	80.5
3, 4	-64.75	77	-64.75	80.5
4	-63	77	-63	80.5
4, 5	-61.25	77	-61.25	80.5
5	-59.5	77	-59.5	80.5
5, 6	-57.75	77	-57.75	80.5
6	-56	77	-56	80.5
6, 7	-54.25	77	-54.25	80.5
7	-52.5	77	-52.5	80.5
7, 8	-50.75	77	-50.75	80.5
8	-49	77	-49	80.5
8, 9	-47.25	77	-47.25	80.5

9	-45.5	77	-45.5	80.5
9, 10	-43.75	77	-43.75	80.5
10	-42	77	-42	80.5
10, 11	-40.25	77	-40.25	80.5
11	-38.5	77	-38.5	80.5
11, 12	-36.75	77	-36.75	80.5
12	-35	77	-35	80.5
12, 13	-33.25	77	-33.25	80.5
13	-31.5	77	-31.5	80.5
13, 14	-29.75	77	-29.75	80.5
14	-28	77	-28	80.5
14, 15	-26.25	77	-26.25	80.5
15	-24.5	77	-24.5	80.5
15, 16	-22.75	77	-22.75	80.5
16	-21	77	-21	80.5
16, 17	-19.25	77	-19.25	80.5
17	-17.5	77	-17.5	80.5
17, 18	-15.75	77	-15.75	80.5
18	-14	77	-14	80.5
18, 19	-12.25	77	-12.25	80.5
19	-10.5	77	-10.5	80.5
19, 20	-8.75	77	-8.75	80.5
20	-7	77	-7	80.5
20, 21	-5.25	77	-5.25	80.5
21	-3.5	77	-3.5	80.5
21, 22	-1.75	77	-1.75	80.5
22	0	77	0	80.5
22, 23	1.75	77	1.75	80.5
23	3.5	77	3.5	80.5
23, 24	5.25	77	5.25	80.5
24	7	77	7	80.5
24, 25	8.75	77	8.75	80.5
25	10.5	77	10.5	80.5
25, 26	12.25	77	12.25	80.5
26	14	77	14	80.5
26, 27	15.75	77	15.75	80.5
27	17.5	77	17.5	80.5
27, 28	19.25	77	19.25	80.5
28	21	77	21	80.5
28, 29	22.75	77	22.75	80.5

29	24.5	77	24.5	80.5
29, 30	26.25	77	26.25	80.5
30	28	77	28	80.5
30, 31	29.75	77	29.75	80.5
31	31.5	77	31.5	80.5
31, 32	33.25	77	33.25	80.5
32	35	77	35	80.5
32, 33	36.75	77	36.75	80.5
33	38.5	77	38.5	80.5
33, 34	40.25	77	40.25	80.5
34	42	77	42	80.5
34, 35	43.75	77	43.75	80.5
35	45.5	77	45.5	80.5
35, 36	47.25	77	47.25	80.5
36	49	77	49	80.5
36, 37	50.75	77	50.75	80.5
37	52.5	77	52.5	80.5
37, 38	54.25	77	54.25	80.5
38	56	77	56	80.5
38, 39	57.75	77	57.75	80.5
39	59.5	77	59.5	80.5
39, 40	61.25	77	61.25	80.5
40	63	77	63	80.5
40, 41	64.75	77	64.75	80.5
41	66.5	77	66.5	80.5
41, 42	68.25	77	68.25	80.5
42	70	77	70	80.5
42, 43	71.75	77	71.75	80.5
43	73.5	77	73.5	80.5

Lookup table for the X- and Y- coordinates of the points in module (3, 1, 1).

	First crystal layer		Second crystal layer	
WLS ID	**X_{scan}**	**Z_{scan}**	**X_{scan}**	**Z_{scan}**
1	77	73.5	80.5	73.5
1, 2	77	71.75	80.5	71.75
2	77	70	80.5	70
2, 3	77	68.25	80.5	68.25
3	77	66.5	80.5	66.5
3, 4	77	64.75	80.5	64.75
4	77	63	80.5	63
4, 5	77	61.25	80.5	61.25
5	77	59.5	80.5	59.5
5, 6	77	57.75	80.5	57.75
6	77	56	80.5	56
6, 7	77	54.25	80.5	54.25
7	77	52.5	80.5	52.5
7, 8	77	50.75	80.5	50.75
8	77	49	80.5	49
8, 9	77	47.25	80.5	47.25
9	77	45.5	80.5	45.5
9, 10	77	43.75	80.5	43.75
10	77	42	80.5	42
10, 11	77	40.25	80.5	40.25
11	77	38.5	80.5	38.5
11, 12	77	36.75	80.5	36.75
12	77	35	80.5	35
12, 13	77	33.25	80.5	33.25
13	77	31.5	80.5	31.5
13, 14	77	29.75	80.5	29.75
14	77	28	80.5	28
14, 15	77	26.25	80.5	26.25
15	77	24.5	80.5	24.5
15, 16	77	22.75	80.5	22.75
16	77	21	80.5	21
16, 17	77	19.25	80.5	19.25
17	77	17.5	80.5	17.5
17, 18	77	15.75	80.5	15.75
18	77	14	80.5	14
18, 19	77	12.25	80.5	12.25

19	77	10.5	80.5	10.5
19, 20	77	8.75	80.5	8.75
20	77	7	80.5	7
20, 21	77	5.25	80.5	5.25
21	77	3.5	80.5	3.5
21, 22	77	1.75	80.5	1.75
22	77	0	80.5	0
22, 23	77	-1.75	80.5	-1.75
23	77	-3.5	80.5	-3.5
23, 24	77	-5.25	80.5	-5.25
24	77	-7	80.5	-7
24, 25	77	-8.75	80.5	-8.75
25	77	-10.5	80.5	-10.5
25, 26	77	-12.25	80.5	-12.25
26	77	-14	80.5	-14
26, 27	77	-15.75	80.5	-15.75
27	77	-17.5	80.5	-17.5
27, 28	77	-19.25	80.5	-19.25
28	77	-21	80.5	-21
28, 29	77	-22.75	80.5	-22.75
29	77	-24.5	80.5	-24.5
29, 30	77	-26.25	80.5	-26.25
30	77	-28	80.5	-28
30, 31	77	-29.75	80.5	-29.75
31	77	-31.5	80.5	-31.5
31, 32	77	-33.25	80.5	-33.25
32	77	-35	80.5	-35
32, 33	77	-36.75	80.5	-36.75
33	77	-38.5	80.5	-38.5
33, 34	77	-40.25	80.5	-40.25
34	77	-42	80.5	-42
34, 35	77	-43.75	80.5	-43.75
35	77	-45.5	80.5	-45.5
35, 36	77	-47.25	80.5	-47.25
36	77	-49	80.5	-49
36, 37	77	-50.75	80.5	-50.75
37	77	-52.5	80.5	-52.5
37, 38	77	-54.25	80.5	-54.25
38	77	-56	80.5	-56
38, 39	77	-57.75	80.5	-57.75

39	77	-59.5	80.5	-59.5
39, 40	77	-61.25	80.5	-61.25
40	77	-63	80.5	-63
40, 41	77	-64.75	80.5	-64.75
41	77	-66.5	80.5	-66.5
41, 42	77	-68.25	80.5	-68.25
42	77	-70	80.5	-70
42, 43	77	-71.75	80.5	-71.75
43	77	-73.5	80.5	-73.5

Lookup table for the X- and Y- coordinates of the possible positions in module (4, 1, 1).

	First crystal layer		**Second crystal layer**	
WLS ID	**X_{scan}**	**Z_{scan}**	**X_{scan}**	**Z_{scan}**
1	73.5	-77	73.5	-80.5
1, 2	71.75	-77	71.75	-80.5
2	70	-77	70	-80.5
2, 3	68.25	-77	68.25	-80.5
3	66.5	-77	66.5	-80.5
3, 4	64.75	-77	64.75	-80.5
4	63	-77	63	-80.5
4, 5	61.25	-77	61.25	-80.5
5	59.5	-77	59.5	-80.5
5, 6	57.75	-77	57.75	-80.5
6	56	-77	56	-80.5
6, 7	54.25	-77	54.25	-80.5
7	52.5	-77	52.5	-80.5
7, 8	50.75	-77	50.75	-80.5
8	49	-77	49	-80.5
8, 9	47.25	-77	47.25	-80.5
9	45.5	-77	45.5	-80.5
9, 10	43.75	-77	43.75	-80.5
10	42	-77	42	-80.5
10, 11	40.25	-77	40.25	-80.5
11	38.5	-77	38.5	-80.5
11, 12	36.75	-77	36.75	-80.5
12	35	-77	35	-80.5

12, 13	33.25	-77	33.25	-80.5
13	31.5	-77	31.5	-80.5
13, 14	29.75	-77	29.75	-80.5
14	28	-77	28	-80.5
14, 15	26.25	-77	26.25	-80.5
15	24.5	-77	24.5	-80.5
15, 16	22.75	-77	22.75	-80.5
16	21	-77	21	-80.5
16, 17	19.25	-77	19.25	-80.5
17	17.5	-77	17.5	-80.5
17, 18	15.75	-77	15.75	-80.5
18	14	-77	14	-80.5
18, 19	12.25	-77	12.25	-80.5
19	10.5	-77	10.5	-80.5
19, 20	8.75	-77	8.75	-80.5
20	7	-77	7	-80.5
20, 21	5.25	-77	5.25	-80.5
21	3.5	-77	3.5	-80.5
21, 22	1.75	-77	1.75	-80.5
22	0	-77	0	-80.5
22, 23	-1.75	-77	-1.75	-80.5
23	-3.5	-77	-3.5	-80.5
23, 24	-5.25	-77	-5.25	-80.5
24	-7	-77	-7	-80.5
24, 25	-8.75	-77	-8.75	-80.5
25	-10.5	-77	-10.5	-80.5
25, 26	-12.25	-77	-12.25	-80.5
26	-14	-77	-14	-80.5
26, 27	-15.75	-77	-15.75	-80.5
27	-17.5	-77	-17.5	-80.5
27, 28	-19.25	-77	-19.25	-80.5
28	-21	-77	-21	-80.5
28, 29	-22.75	-77	-22.75	-80.5
29	-24.5	-77	-24.5	-80.5
29, 30	-26.25	-77	-26.25	-80.5
30	-28	-77	-28	-80.5
30, 31	-29.75	-77	-29.75	-80.5
31	-31.5	-77	-31.5	-80.5
31, 32	-33.25	-77	-33.25	-80.5
32	-35	-77	-35	-80.5

32, 33	-36.75	-77	-36.75	-80.5
33	-38.5	-77	-38.5	-80.5
33, 34	-40.25	-77	-40.25	-80.5
34	-42	-77	-42	-80.5
34, 35	-43.75	-77	-43.75	-80.5
35	-45.5	-77	-45.5	-80.5
35, 36	-47.25	-77	-47.25	-80.5
36	-49	-77	-49	-80.5
36, 37	-50.75	-77	-50.75	-80.5
37	-52.5	-77	-52.5	-80.5
37, 38	-54.25	-77	-54.25	-80.5
38	-56	-77	-56	-80.5
38, 39	-57.75	-77	-57.75	-80.5
39	-59.5	-77	-59.5	-80.5
39, 40	-61.25	-77	-61.25	-80.5
40	-63	-77	-63	-80.5
40, 41	-64.75	-77	-64.75	-80.5
41	-66.5	-77	-66.5	-80.5
41, 42	-68.25	-77	-68.25	-80.5
42	-70	-77	-70	-80.5
42, 43	-71.75	-77	-71.75	-80.5
43	-73.5	-77	-73.5	-80.5